Bistable superlattice switching in a quantum spin Hall insulator

https://doi.org/10.1038/s41586-026-10309-w

Received: 8 June 2025

Accepted: 20 February 2026

Jian Tang[1], Thomas Siyuan Ding[1], Shuhan Ding[2], Jiangxu Li[3,4], Changjiang Yi[1,5], Tianxing Tang[1], Zumeng Huang[1], Xuehao Wu[6], Zhiheng Huang[1], Birender Singh[1], Tiema Qian[7], Vsevolod Belosevich[1], Mingyang Guo[1], Anyuan Gao[8], Nikolai Peshcherenko[5], Zhe Sun[1,8], Mohamed Shehabeldin[1], Kenji Watanabe[9], Takashi Taniguchi[10], Abhay N. Pasupathy[6,11], Claudia Felser[5], Kenneth S. Burch[1], Ni Ni[7], Yao Wang[2], Yang Zhang[3,4], Su-Yang Xu[8] & Qiong Ma[1,12]✉

Bistable switching typically arises from ferroic orders, such as ferroelectricity and ferromagnetism, in which the bistable states are encoded in charge or spin degrees of freedom[1,2]. Here we report the observation of bistable superlattice switching in monolayer $TaIrTe_4$, a dual quantum spin Hall insulator[3–5]. Switching occurs between two lattice configurations with sharply contrasting periodicities. In particular, in a pristine monolayer, we observe the spontaneous emergence of a long-period superlattice that can be programmed on and off in a non-volatile manner by electrostatic tuning of low-energy electronic states. This switching toggles the system between two structural configurations with unit cell areas differing by two orders of magnitude. Mechanistically, our results reveal two independent and distinct instabilities, one in the lattice and the other in the quantum spin Hall electrons. These instabilities are coupled, leading to electrostatic control of lattice configurations with non-volatile memory. This finding is enabled by combining linear and nonlinear transport measurements[6–13], Raman spectroscopy and scanning tunnelling microscopy, which probe complementary aspects of the underlying orders. Notably, this non-volatile memory stabilizes a spontaneous superlattice with a periodicity on the few-nanometre scale that remains robust across a wide doping range, persists over days and survives above 70 K. Our preliminary data also show the emergence of new insulating states at fractional superlattice fillings, which can be switched on and off together with the superlattice.

In solids, memory phenomena often originate from spontaneous symmetry breaking. For example, the breaking of spatial inversion and time-reversal symmetries gives rise to ferroelectricity and magnetism[1,2], respectively (Fig. 1a,b), where the associated charge and spin degrees of freedom serve as information carriers. Beyond charge and spin, the lattice configuration itself constitutes a fundamental degree of freedom, one governed by translational symmetry breaking and manifested in the (approximate) periodicity of the crystal lattice. This underlying periodicity defines the intrinsic length and energy scales of a material and sets the stage for its electronic structure and related phenomena. Recent breakthroughs with moiré superlattices have shown that periodicities of several nanometres can produce flat electronic bands, thus enabling a range of exotic quantum phenomena[14–29]. Realizing the memory control of superlattices, therefore, naturally enables the memory control of these quantum phenomena and may lead to new classes of memory technologies[30], which have been lacking[31–37].

Here we report the observation of a non-volatile 'superlattice memory', simply using an electrostatic gating (Fig. 1c). Specifically, in the absence of a predefined superlattice structure—whether fabricated or grown—we observe, upon cooling, the spontaneous formation of a superlattice in monolayer $TaIrTe_4$, a recently identified dual quantum spin Hall (QSH) insulator[5]. This superlattice can be reversibly switched on and off by tuning the low-energy QSH electrons. This toggles the system between an atomic lattice (unit cell area approximately 0.47 nm^2) and a superlattice (supercell area approximately 62 nm^2). In the context of charge-density-wave (CDW) systems and their memory and control[38–42], the memory here resides exclusively in the lattice order. Moreover, the electronic order can be independently controlled within each lattice memory state. All these states

---

[1] Department of Physics, Boston College, Chestnut Hill, MA, USA. [2] Department of Chemistry, Emory University, Atlanta, GA, USA. [3] Department of Physics and Astronomy, University of Tennessee, Knoxville, TN, USA. [4] Min H. Kao Department of Electrical Engineering and Computer Science, University of Tennessee, Knoxville, TN, USA. [5] Max Planck Institute for Chemical Physics of Solids, Dresden, Germany. [6] Department of Physics, Columbia University, New York, NY, USA. [7] Department of Physics and Astronomy and California NanoSystems Institute, University of California Los Angeles, Los Angeles, CA, USA. [8] Department of Chemistry and Chemical Biology, Harvard University, Cambridge, MA, USA. [9] Research Center for Electronic and Optical Materials, National Institute for Materials Science, Tsukuba, Japan. [10] Research Center for Materials Nanoarchitectonics, National Institute for Materials Science, Tsukuba, Japan. [11] Condensed Matter Physics and Materials Science Division, Brookhaven National Laboratory, Upton, NY, USA. [12] The Schiller Institute for Integrated Science and Society, Boston College, Chestnut Hill, MA, USA. ✉e-mail: maqa@bc.edu

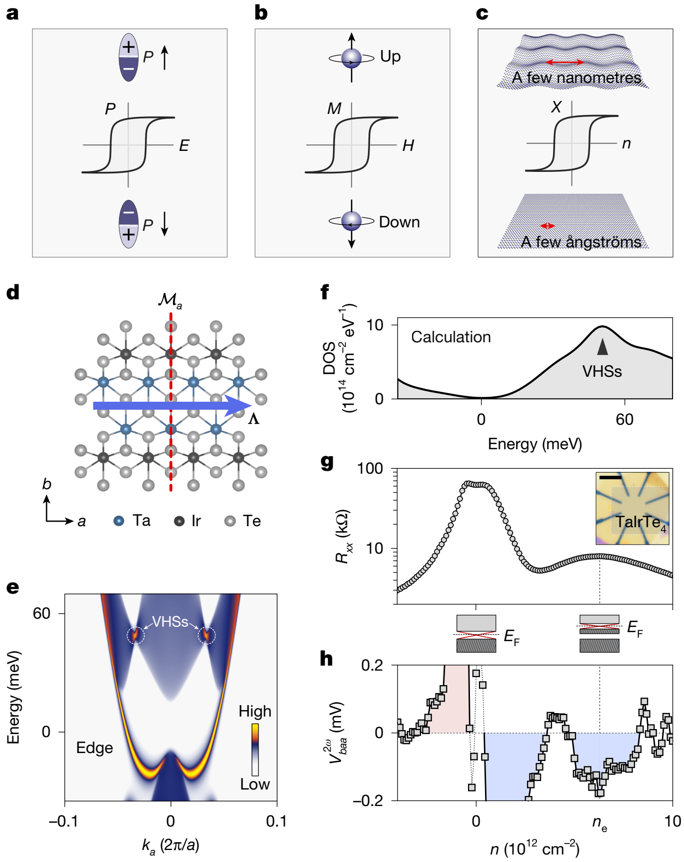

Fig. 1 | Nonlinear Hall characterization of the dual QSH state in monolayer TaIrTe$_4$. **a**–**c**, Illustrations of the charge (**a**), spin (**b**) and superlattice (**c**) memories. **d**, Top view of the atomic lattice structure with a mirror plane $\mathcal{M}_a$, which permits a Berry curvature dipole $\boldsymbol{\Lambda}$ along $\hat{a}$. **e**, Calculated spectral weight projected along k_a, showing QSH edge states within the bulk bandgap and VHSs in the bulk conduction band. **f**, Calculated density of states (DOS) versus energy. A large DOS is observed at the VHSs. **g**, The linear resistance R_{xx} as a function of carrier density n at $T = 4$ K (sharing the same x axis as **h**). Two resistance peaks are observed corresponding to the single-particle bandgap ($n = 0$, charge neutral point (CNP), see the left schematic below the x axis) and the correlated bandgap ($n = n_e$, see the right schematic below the x axis), respectively. Inset, optical image of device 1. **h**, The second-order (2ω) nonlinear Hall voltage $V_{baa}^{2\omega}$ versus n, measured with an a.c. current $I^{\omega} = 1$ μA at $\omega = 17.777$ Hz and $T = 4$ K. Large $V_{baa}^{2\omega}$ responses are observed near the CNP and n_e. The positive and negative $V_{baa}^{2\omega}$ responses are shaded by red and blue, respectively. Scale bar, 5 μm (inset in **g**). P, polarization; E, electric field; M, magnetization; H, magnetic field; X, lattice order; k_a, wavevector along $\hat{a}$; E_F, Fermi level.

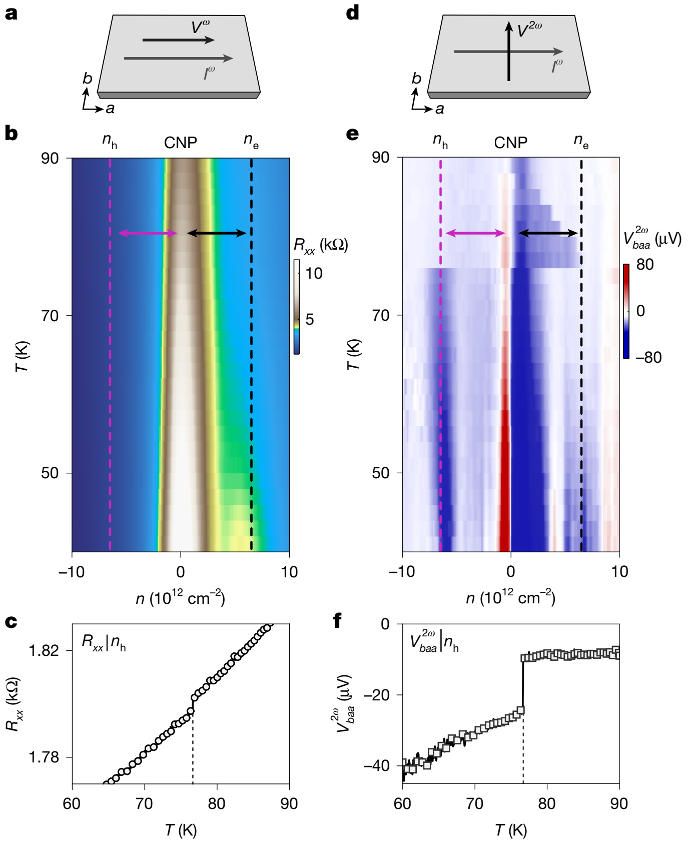

Fig. 2 | Observation of a hidden state beyond the dual QSH state. **a**, Schematic of the linear transport setup. **b**, Linear resistance R_{xx} as a function of carrier density n and temperature T during warm-up from 40 K. Resistance peaks are observed at the CNP and at n_e, corresponding to the single-particle and correlated QSH gaps, respectively. As the temperature increases from 4 K to 40 K, the correlated-gap peak shifts to lower carrier density; consequently, n_e appears slightly right of the resistance peak in this panel (Extended Data Fig. 3a). **c**, Temperature dependence of R_{xx} measured at fixed density $n = n_h$ ($R_{xx}|n_h$) during the warm-up (magenta dashed line in **b**). **d**, Schematic of the nonlinear Hall transport setup. **e**, Nonlinear Hall voltage $V_{baa}^{2\omega}$ measured simultaneously with the data in **b**. **f**, Temperature dependence of $V_{baa}^{2\omega}$ measured simultaneously with the data in **c** at n_h ($V_{baa}^{2\omega}|n_h$) (magenta dashed line in **e**). The detection sensitivity of $V_{baa}^{2\omega}$—defined as the normalized jump across the transition—is 45%, compared with just 0.13% in R_{xx}, highlighting the enhanced sensitivity of nonlinear Hall measurements in revealing the hidden state. Further data and analysis are presented in Extended Data Figs. 2 and 3. V^{ω}, first-order voltage; $V^{2\omega}$, second-order voltage.

are long-lived under (quasi-)equilibrium conditions. Our findings raise the possibility of realizing lattice-memory control of correlated topological states.

Dual QSH state

Structurally, TaIrTe$_4$ consists of alternating Ta and Ir atomic chains running along the crystallographic $\hat{a}$ axis, with a mirror plane $\mathcal{M}_a$ perpendicular to $\hat{a}$ (Fig. 1d). Electronically, monolayer TaIrTe$_4$ was predicted to be a QSH insulator (Fig. 1e). Recent experimental progress reveals a dual QSH state[5] that extends beyond previous theoretical predictions[3,4]. As shown in ref. 5 and also reproduced in this work (for example, Fig. 1f,g), the dual QSH behaviour manifests as follows. At charge neutrality, the system exhibits a QSH insulating state consistent with single-particle band structure calculations. Upon electron doping, a second insulating peak emerges. We label the density of this peak as n_e and find $n_e \approx 6.5 \times 10^{12}$ cm^{-2} (Fig. 1g). This second insulating state, identified as a correlated QSH phase[5], arises from Van Hove singularities (VHSs) in the conduction band (Fig. 1e).

We investigate the nonlinear Hall effect, which probes the Fermi-surface Berry curvature dipole[6–13,43–45]. The lattice symmetry of TaIrTe$_4$ permits a Berry curvature dipole $\boldsymbol{\Lambda}$ along $\hat{a}$. According to theory[6], applying I^{ω} along $\boldsymbol{\Lambda}$ ($\hat{a}$ axis) generates a second-order Hall voltage $V_{baa}^{2\omega}$ along $\hat{b}$. This nonlinear Hall response is expected to be enhanced near the QSH gaps due to concentrated Berry curvature hotspots. Consistent with this expectation, our measurements reveal prominent $V_{baa}^{2\omega}$ signals near both QSH gaps (Fig. 1h). We further establish its connection to the Berry curvature dipole through systematic investigations in Methods, Extended Data Fig. 1 and Supplementary Information sections 2–5.

Observation of a hidden state

We now explore a broader density range and its temperature dependence during the warm-up. The dual QSH states at $n = 0$ and n_e are again

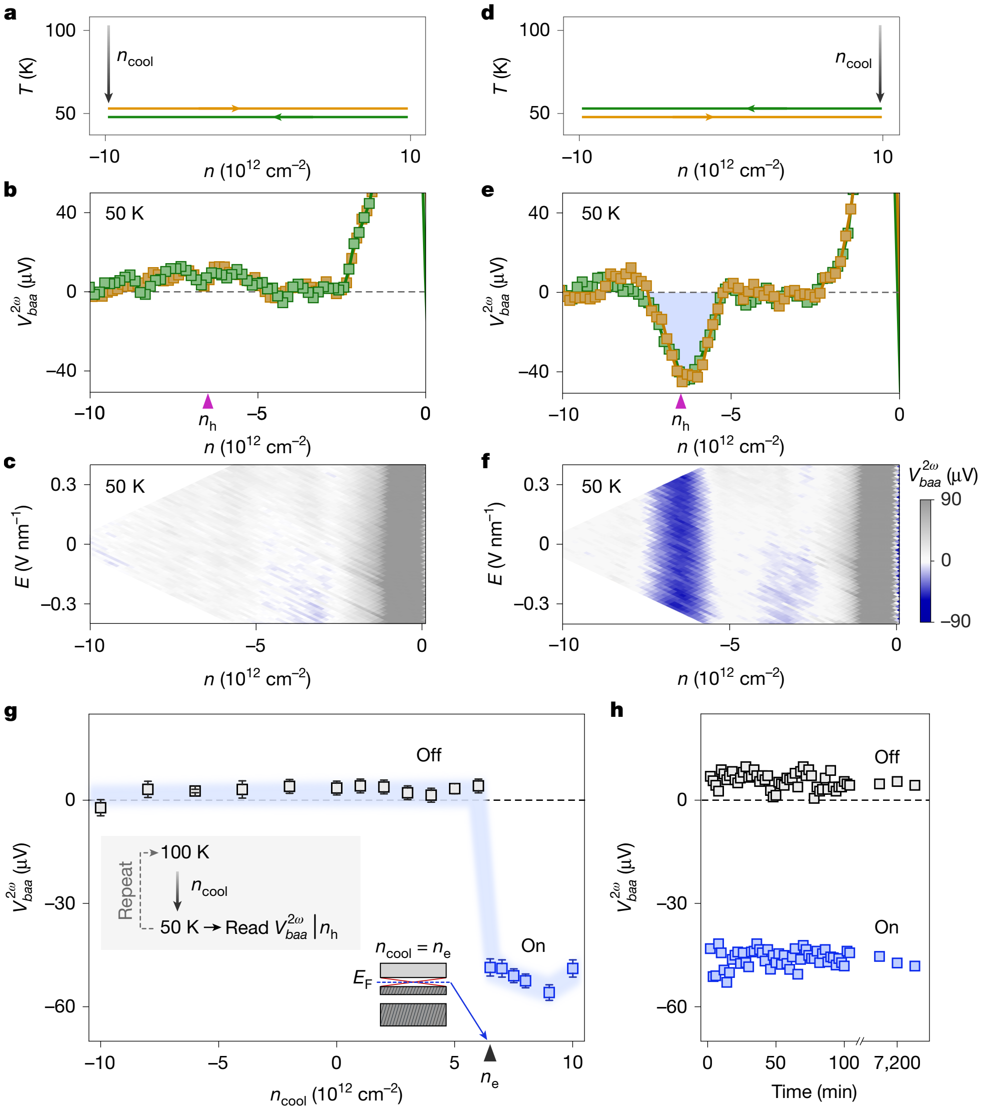

Fig. 3 | Memory effect of the hidden state revealed by cooling-dependent protocols. a–**c**, Cooling process 1. The sample is cooled from 100 K to 50 K at a fixed doping level of $n_{cool} = -10\times10^{12}$ cm^{-2}, followed by $V^{2\omega}_{baa}$ measurements at 50 K during both forward (orange) and backward (green) doping scans (**a**). The signal $V^{2\omega}_{baa}|n_h$ remains negligible (off state) (**b**) and shows no dependence on the perpendicular electric field E (**c**). **d**–**f**, Cooling process 2. Same as in **a** but with $n_{cool} = +10\times10^{12}$ cm^{-2} (**d**). At 50 K, $V^{2\omega}_{baa}|n_h$ exhibits a strong response (on state) (**e**), again independent of E (**f**). **g**, Summary of $V^{2\omega}_{baa}|n_h$ responses at 50 K across several cooling cycles with various n_{cool} values. A critical doping threshold, $n_{cool} = n_e$, corresponding to the carrier density of the correlated QSH gap, is identified—above which the hidden state is activated. Error bars represent the standard deviation of five independent measurements. **h**, Both on and off states of $V^{2\omega}_{baa}|n_h$ persisted for several days, limited only by the duration of our measurement.

readily identified in Fig. 2a,b in R_{xx} and in Fig. 2d,e in $V^{2\omega}_{baa}$. Importantly, beyond these, we observe a new feature in $V^{2\omega}_{baa}$ on the hole-doped side. We label the density of this feature in Fig. 2e as n_h and find $n_h \approx -n_e \approx -6.5\times10^{12}$ cm^{-2}. This n_h feature, denoted as $V^{2\omega}_{baa}|n_h$, emerges sharply below 76 K (Fig. 2f), and we refer to it as the hidden state. A similar jump is also visible in $R_{xx}|n_h$ (Fig. 2c) with less sensitivity. We also note that although $V^{2\omega}_{baa}|n_h$ is reliably reproduced across several devices, its behaviour below 40 K is not entirely consistent, indicating that there are other device-dependent effects (Extended Data Fig. 3). Below, we focus on the consistent behaviour above 40 K.

Memory effect of the hidden state

Interestingly, the hidden state is highly sensitive to the doping level during the cool-down. We fix the carrier density during cooling, denoted as n_{cool}, and cool the sample from 100 K to 50 K. After reaching 50 K, we read out the hidden state through $V^{2\omega}_{baa}|n_h$. When the sample is cooled under $n_{cool} = -10\times10^{12}$ cm^{-2} (Fig. 3a), the hidden state $V^{2\omega}_{baa}|n_h$ is absent (Fig. 3b,c). By contrast, cooling under $n_{cool} = +10\times10^{12}$ cm^{-2} (Fig. 3d) results in a robust $V^{2\omega}_{baa}|n_h$ (Fig. 3e,f). These contrasting outcomes demonstrate that the hidden state is not a simple state function of temperature and doping but, instead, depends on the history of the system as it reflects a memory effect.

We next repeat the cool-down while varying n_{cool} stepwise and read out $V^{2\omega}_{baa}|n_h$ at 50 K (Fig. 3g). The results reveal a critical value of n_{cool} that coincides with n_e. This correspondence points to a close connection between the hidden state at n_h and the correlated QSH phase at n_e. Note that when the system is cooled to 50 K and maintained below this temperature, the presence or absence of the hidden state becomes fixed and cannot be switched. This phenomenon exhibits long retention times of at least several days and is limited only by the duration of our measurements (Fig. 3h).

We now investigate whether doping can directly toggle the hidden state. We fix the temperature at $T = 70$ K, slightly below the onset

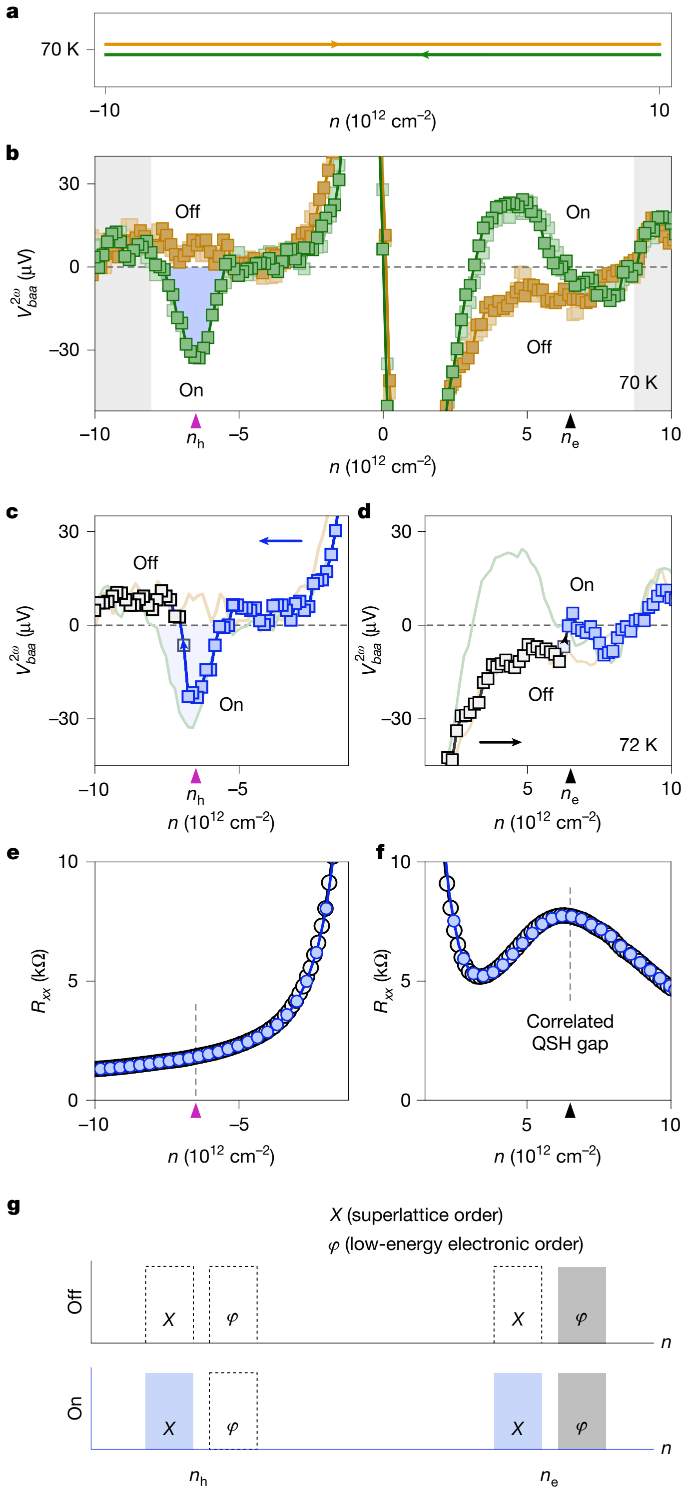

Fig. 4 | Direct doping switch of the hidden state and observation of superlattice memory. a,**b**, Schematic illustration (**a**) and the corresponding measurement results of forward and backward doping scans of $V^{2\omega}_{baa}$ at $T = 70$ K (**b**). The results demonstrate that the hidden state at n_h can be reversibly switched on and off by doping alone. The switching is highly reproducible, as evidenced by two overlapping measurement cycles (green and light green; orange and light orange). **c**,**d**, Identification of erase (on (blue) → off (black)) (**c**) and write (off (black) → on (blue)) (**d**) transitions of the hidden state at $T = 72$ K. Background data from $T = 70$ K (orange and green) are shown for comparison. **e**, R_{xx} near n_h at $T = 4$ K for the on (blue circles) and off (black circles) states. **f**, R_{xx} near n_e at $T = 4$ K for the on (blue circles) and off (black circles) states. The correlated QSH gap at n_e remains robust in both cases. **g**, The hidden state corresponds to a superlattice order X that exhibits on and off configurations at both n_e and n_h, whereas the low-energy electronic order φ is always on at n_e and always off at n_h.

temperature of 76 K, and scan the carrier density n in both forward and backward directions (Fig. 4a). The data reveal clear hysteresis (Fig. 4b): the hidden state is on when scanning n backwards and off when scanning forwards, thereby directly demonstrating the memory effect. We note that the on and off of the hidden state at n_h are accompanied by a noticeable and highly reproducible change in the features at n_e. This indicates that the order responsible for the response at n_h also exhibits on and off states at n_e, a point that will be important for later discussions.

Direct doping hysteresis is observed between approximately 72 K and approximately 60 K, as shown in Extended Data Fig. 4. At each temperature, a critical 'write' density can be identified at which the hidden state switches from off to on. For example, at $T = 72$ K, the transition occurs near n_e during the forward scan, as indicated by the black arrow in Fig. 4d. At this point, the off-state data (black squares), consistent with the orange squares in Fig. 4b, transition to the on-state data (blue squares), matching the green squares in Fig. 4b. Repeating this procedure at different temperatures allows us to map the critical write density and construct the writing boundary shown in Fig. 6a. As the system is cooled further, the write density shifts towards higher electron doping. Below 58 K, switching from off to on is no longer achievable within the accessible doping range, indicating that the writing force becomes insufficient to drive the transition.

A similar method can be used to identify the 'erase' density of the hidden state. At 72 K (Fig. 4c), we observe a jump from the on to the off state near n_h (blue arrow) when scanning n backwards. As the system is cooled, the erase threshold shifts towards higher hole doping. However, in this device, $V^{2\omega}_{baa}|n_\mathrm{h}$ in the on state is narrowly confined near n_h, such that away from n_h the distinction between on and off states becomes negligible. This limits the number of data points available for precisely determining the erase boundary. Below 61 K, the state can no longer be switched from on to off within the accessible doping range, making the maximum hole doping another boundary point at 61 K. We note that this narrowness of $V^{2\omega}_{baa}|n_\mathrm{h}$ is not universal: in another device, a wider doping-range response allows the erase boundary to be determined more precisely (Extended Data Fig. 4).

We also find from R_{xx} that the correlated QSH state at n_e is always on, regardless of the hidden state (Fig. 4e,f and Extended Data Fig. 5). By contrast, the hidden state—revealed by $V^{2\omega}_{baa}$—exhibits clear on and off behaviour that depends on the temperature and doping history, with pronounced signatures not only at n_h but also at n_e (Fig. 4b,d).

The hidden state is a superlattice

We summarize the key experimental observations and their immediate implications. Observation 1: We observe a large $V^{2\omega}_{baa}|n_\mathrm{h}$ only below 76 K (Fig. 2e), indicating a new ordered phase that reconstructs the electronic structure and Berry curvature near n_h. Observation 2: We find that $n_\mathrm{h} \approx -n_\mathrm{e}$. Observation 3: The emergence of $V^{2\omega}_{baa}|n_\mathrm{h}$ depends strongly on the doping history and is triggered by doping through n_e. Together with the relation $n_\mathrm{h} \approx -n_\mathrm{e}$, this points to an intrinsic connection between the hidden state and the correlated QSH state at n_e. Observation 4: The on and off switching of $V^{2\omega}_{baa}|n_\mathrm{h}$ is accompanied by a highly reproducible hysteretic change in $V^{2\omega}_{baa}|n_\mathrm{e}$, indicating that the hidden state also switches on and off near n_e (Fig. 4b). By contrast, the linear resistance R_{xx} consistently exhibits a peak at n_e (Fig. 4e,f), demonstrating that the correlated QSH insulating state at n_e remains robustly on.

We now examine several possible interpretations. Possibility 1: $V^{2\omega}_{baa}|n_\mathrm{h}$ arises from charge trapping by defects or impurities, which can produce hysteresis and memory effects. However, this scenario cannot readily

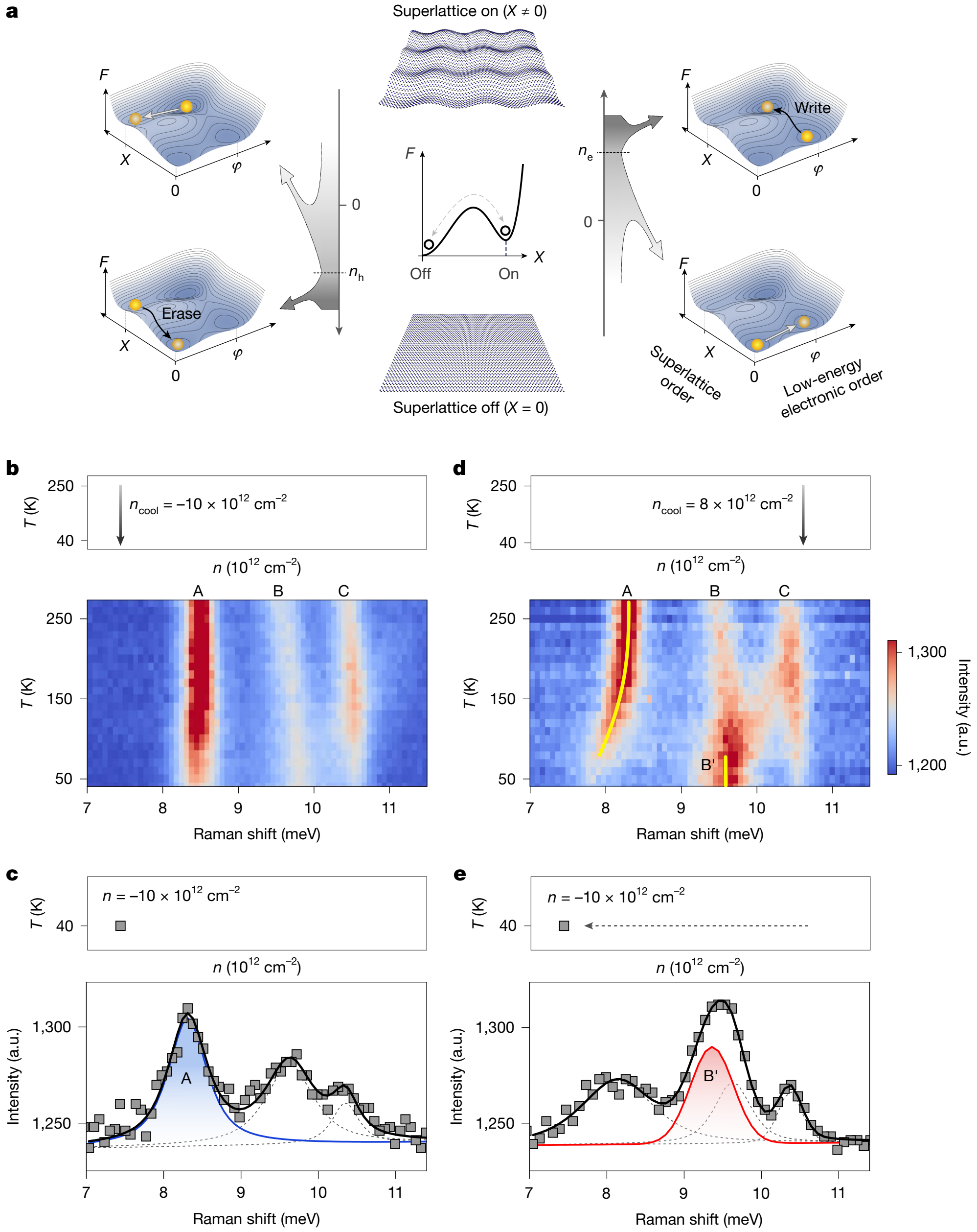

Fig. 5 | Electronically driven superlattice and Raman signature of two lattice states. a, Schematic of superlattice switching. Doping tunes the system between $X = 0$ and $X \neq 0$ through coupling to φ, thus driving transitions across local minima in the φ–X free-energy (F) landscape. Technically, this occurs through deformation or tilting of the landscape. For example, as n approaches n_e, the minimum shifts from $\varphi = 0$ to $\varphi \neq 0$. We simplify this process with an effective arrow. A more rigorous analysis is provided in Supplementary Information section 5. **b**, Raman spectra taken while cooling the sample from 270 K to 40 K at $n_{cool} = -10 \times 10^{12}$ cm^{-2}, corresponding to programming the system into the superlattice off state. **c**, The spectrum at $T = 40$ K and $n = -10 \times 10^{12}$ cm^{-2}. **d**, Raman spectra taken while cooling the sample from 270 K to 40 K at $n_{cool} = 8 \times 10^{12}$ cm^{-2}, corresponding to programming the system into the superlattice on state. During cooling, peak A softens and a new peak, denoted B′, emerges. **e**, The spectrum at $T = 40$ K after tuning the doping from $n_{cool} = 8 \times 10^{12}$ cm^{-2} to $n = -10 \times 10^{12}$ cm^{-2}. The B′ mode persists. The top panels of **b**–**e** show schematics of the measurement conditions, with the results shown below. a.u., arbitrary units.

explain the sharp temperature onset or the relation $n_h \approx -n_e$. Possibility 2: $V^{2\omega}_{baa}|n_h$ originates from an unintentional superlattice formed between TaIrTe$_4$ and the boron nitride substrate. This could account for $n_h \approx -n_e$, as these densities would correspond to full electron and hole fillings of the same superlattice unit cell. In this case, however, the values of n_e and n_h would be sample dependent and vary with the relative rotational alignment. By contrast, all devices studied here consistently show $n_h \approx -n_e \approx -6.5 \times 10^{12}$ cm^{-2}. Moreover, this scenario is inconsistent with the observed memory effect and the sharp temperature onset. Possibility 3: $V^{2\omega}_{baa}|n_h$ arises from the same underlying order responsible for the correlated QSH state at n_e, for example, a charge order driven by the VHSs. This could explain the relation $n_h \approx -n_e$ and potentially account for the temperature onset and memory behaviour. However, this interpretation conflicts with observation 4: the correlated QSH state at n_e is always on. If the feature at n_h originated from the same order, it should likewise remain on at n_e. Instead, $V^{2\omega}_{baa}$ clearly reveals two distinct states near n_e that switch in concert with the state at n_h (Fig. 4b,d).

Although we do not claim to have exhausted all possibilities, we propose a phenomenological framework (our possibility 4) that naturally accounts for our observations. We introduce a low-energy electronic order parameter φ, which characterizes the correlated

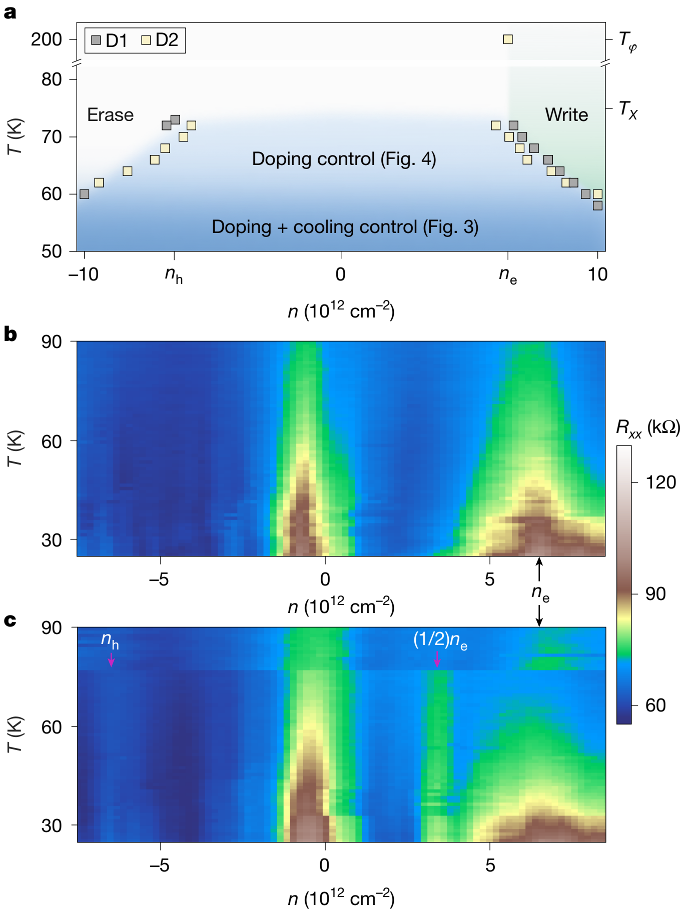

Fig. 6 | Experimental control diagram and emergence of fractional superlattice filling states with memory. a, Experimental control diagram. T_φ and T_X denote the critical temperatures of the electronic (φ) and lattice (X) orders, respectively. T_X is determined from the temperature dependence of $V^{2\omega}_{baa}$ at n_h (Fig. 2f), whereas T_φ is determined from the temperature dependence of R_{xx} at n_e (Supplementary Information section 12). Cooling from the write region (green) switches the superlattice to the on state, whereas cooling from the erase region (white) sets it to the off state. In the doping plus cooling control region (blue), the state is locked by temperature. In the doping control region (light blue), it can be reversibly switched by doping alone (Figs. 3 and 4). **b**,**c**, In device 2, the same programming protocol is applied to set the sample into the superlattice off (**b**) and on (**c**) states (see Supplementary Information section 5 for further characterizations). The linear resistance R_{xx} maps as a function of carrier density n and temperature T are measured during warming in the off state and on state, respectively. The on state exhibits a weak resistance peak at n_h, and another distinct peak appears near the filling approximately $n_e/2$, which vanishes sharply around 75 K together with the n_h feature.

insulating phase at n_e. This order, which may be a CDW, emerges as doping approaches the VHSs. In parallel, we introduce a lattice order parameter X, which takes two values: $X \neq 0$ denotes the presence of a superlattice that breaks the same translational symmetry as φ, whereas $X = 0$ corresponds to its absence. Figure 4g summarizes the states of these two order parameters near n_e and n_h. Their connection to the R_{xx} and $V^{2\omega}_{baa}$ responses are explained in Extended Data Fig. 6. From Fig. 4g, the observed memory effect is encoded in the order parameter X, a lattice memory.

Two instabilities

Figure 4g illustrates that the electronic and lattice orders (φ, X) are independent instabilities that can exist separately, rather than co-emerging or co-vanishing as in typical CDW systems. Moreover, the X on state is triggered by the onset of φ (Fig. 3), indicating a coupling between them. We now describe this behaviour with a phenomenological Ginzburg–Landau model:

$$\begin{aligned}
&F(\varphi, X; T, n) = F_{\text{Lattice}}(X) + F_{\text{Electron}}(\varphi) + F_{\text{Coupling}}(\varphi, X),\\
&F_{\text{Lattice}}(X; T) = \frac{1}{2}\alpha(T)X^2 + \frac{1}{4!}\beta(T)X^4 + \frac{1}{6!}X^6,\\
&F_{\text{Electron}}(\varphi; T, n) = \frac{1}{2}a(T, n)\varphi^2 + \frac{1}{4!}\varphi^4,\\
&F_{\text{Coupling}}(\varphi, X) = \lambda\varphi X.
\end{aligned} \tag{1}$$

Here, λ is the electron–lattice coupling coefficient. A full analysis of this model and its ability to reproduce the control diagram in Fig. 6a are presented in Methods (where the coefficients of $\alpha(T)$, $\beta(T)$ and $a(T, n)$ are defined) and Supplementary Information section 5. Here we highlight several key features. First, the functional forms of $F_{\text{Electron}}(\varphi)$ and $F_{\text{Lattice}}(X)$ can support independent local minima at non-zero φ and X, respectively, as illustrated in Extended Data Fig. 7. $F_{\text{Electron}}(\varphi)$ exhibits a single minimum—either at $\varphi = 0$ or $\varphi \neq 0$ (up to sign)—set by doping. By contrast, $F_{\text{Lattice}}(X)$, modelled as a sixth-order polynomial, supports two coexisting minima at $X = 0$ and $X \neq 0$ (also up to sign), separated by a finite energy barrier. The coupling term $\lambda\varphi X$ allows doping to tilt the free-energy landscape of X and modulate this barrier. The energy barrier is essential for decoupling the dynamics of X from φ (Extended Data Fig. 8): once established, X can remain trapped in either the $X = 0$ or $X \neq 0$ minimum, independent of the current state of φ. Below, we use this model to describe the observations in Figs. 3 and 4:

(1) Doping-induced superlattice switching during cooling (Fig. 3): As the system cools through the superlattice transition temperature T_X—set by $F_{\text{Lattice}}(X)$—the barrier between $X = 0$ and $X \neq 0$ is minimal, allowing the weak writing force F_{write} to favour $X \neq 0$. For $n < n_e$, $\varphi = 0$ and the coupling vanishes, keeping the system at $X = 0$. For $n > n_e$, $\varphi \neq 0$ activates the coupling, favouring $X \neq 0$. As cooling proceeds, the barrier grows and locks in the selected state. See Extended Data Fig. 9 for illustrations.

(2) Doping-induced superlattice switching without cooling (Fig. 4): Following Fig. 5a and starting from $n = 0$, the system resides in the $\varphi = 0$ and $X = 0$ minimum. As n increases towards n_e, φ turns on, and the coupling term generates a writing force F_{write} that overcomes the energy barrier, switching the system to $X \neq 0$. The required writing density increases at lower temperatures (Fig. 6a), indicating that higher electron doping is needed to generate a sufficient writing force to overcome the growing energy barrier. Upon reversing the doping, φ vanishes, but the system remains trapped in the $X \neq 0$ state. The return transition occurs near n_h, shifting towards higher hole doping at lower temperatures (Fig. 6a). This indicates that higher hole doping generates a larger erasing force. The microscopic mechanism by which doping influences the writing or erasing force remains to be explored. Once erased, the system remains in the $X = 0$ state until F_{write} again exceeds the barrier, thus completing the hysteresis loop. See more discussions in the Methods.

Raman signature of two lattice states

We now present the Raman data. The sample was first cooled to 40 K at $n_{\text{cool}} = -10 \times 10^{12}$ cm^{-2} (superlattice off). The Raman spectrum in the 7–11 meV range exhibits three modes—labelled A, B and C—that remain largely unchanged upon cooling (Fig. 5b,c). By contrast, upon cooling at $n_{\text{cool}} = 8 \times 10^{12}$ cm^{-2} (superlattice on), mode A begins to soften and broaden near approximately 200 K and becomes very weak below approximately 76 K (Fig. 5d). One possible origin of this softening and broadening is strong electron–phonon coupling (see the discussion in Supplementary Information section 12). Simultaneously, another mode (labelled B′) emerges just below the energy of the B mode. Further evidence supporting B′ as a distinct Raman mode is provided in Extended Data Fig. 10. When the system is held at 40 K and the doping is tuned from 8×10^{12} cm^{-2} to -10×10^{12} cm^{-2}—the same doping and temperature as in Fig. 5c—the B′ mode persists (Fig. 5e). These Raman results, therefore, reveal two distinct lattice states that depend on the doping and cooling history.

Interestingly, a recent study[13] reported CDW transitions in few-layer $TaIrTe_4$ using nonlinear Hall and Raman, indicating that CDW phases are a prevailing feature of $TaIrTe_4$ from monolayer[5] to multilayers. What we demonstrate here is different: an electronically driven lattice memory. Both nonlinear Hall and Raman reveal two lattice states that can be non-volatilely switched by tuning the low-energy electronic states.

Emergent state at half filling

This non-volatile memory stabilizes a spontaneous superlattice that remains robust across a wide doping range, persists for days (limited only by measurement duration) and survives temperatures above 70 K. See discussions regarding further performance metrics and future prospects in Supplementary Information sections 9, 13 and 14. Moreover, by combining transport data with preliminary scanning tunnelling microscopy results, we estimate the supercell area to be approximately 62 nm^2 (Supplementary Information sections 10 and 11), comparable with that of flat-band moiré systems.

Combined with the QSH topology, this platform presents a promising route to realizing exotic correlated phases. In device 2, we employ the same doping–cooling programming protocol to set the system into the superlattice off (Fig. 6b) and on (Fig. 6c) states. In the on state, we directly observe a weak but discernible linear resistance peak at n_h, further supporting our interpretation of a superlattice-induced gap at n_h. Strikingly, another resistance peak emerges near $n_e/2$, which is unique to the on state and vanishes—together with the n_h peak—abruptly at approximately 75 K. These observations point to a filling-enabled correlated insulating phase within the superlattice flat band. Possibilities include CDW with longer periodicity, Mott, Stoner-type instability and fractional QSH[46–48]. These represent compelling directions for future investigation.

Discussion and outlook

CDW-related memory phenomena, electronic and lattice instabilities, and electron–lattice coupling have been reported in transition-metal dichalcogenides, kagome metals and cuprates among others[38–42,49,50]. What distinguishes our system is, probably, twofold. On one hand, independent electronic and lattice instabilities, with the energy barrier and electron–lattice coupling operating at comparable energy scales, are delicately balanced within the free-energy landscape. On the other hand, the monolayer and semimetallic nature enables continuous and selective tuning of the electronic state through doping. Together, these features allow the electronic and lattice orders to be independently accessed, tuned and stabilized in quasi-equilibrium, with the memory residing exclusively in the lattice sector. This enables new steady-state functionalities and investigation using experimental equilibrium probes.

Online content

Any methods, additional references, Nature Portfolio reporting summaries, source data, extended data, supplementary information, acknowledgements, peer review information; details of author contributions and competing interests; and statements of data and code availability are available at https://doi.org/10.1038/s41586-026-10309-w.

1. Auciello, O., Scott, J. F. & Ramesh, R. The physics of ferroelectric memories. *Phys. Today* **51**, 22–27 (1998).
2. Chikazumi, S. & Graham, C. D. *Physics of Ferromagnetism* Vol. 94 (Oxford Univ. Press, 1997).
3. Liu, J., Wang, H., Fang, C., Fu, L. & Qian, X. Van der Waals stacking-induced topological phase transition in layered ternary transition metal chalcogenides. *Nano Lett.* **17**, 467–475 (2017).
4. Guo, P.-J., Lu, X.-Q., Ji, W., Liu, K. & Lu, Z.-Y. Quantum spin Hall effect in monolayer and bilayer $TaIrTe_4$. *Phys. Rev. B* **102**, 041109 (2020).
5. Tang, J. et al. Dual quantum spin Hall insulator by density-tuned correlations in $TaIrTe_4$. *Nature* **628**, 515–521 (2024).
6. Sodemann, I. & Fu, L. Quantum nonlinear Hall effect induced by Berry curvature dipole in time-reversal invariant materials. *Phys. Rev. Lett.* **115**, 216806 (2015).
7. Ma, Q. et al. Observation of the nonlinear Hall effect under time-reversal-symmetric conditions. *Nature* **565**, 337–342 (2019).
8. Kang, K., Li, T., Sohn, E., Shan, J. & Mak, K. F. Nonlinear anomalous Hall effect in few-layer WTe_2. *Nat. Mater.* **18**, 324–328 (2019).
9. Xiao, J. et al. Berry curvature memory through electrically driven stacking transitions. *Nat. Phys.* **16**, 1028–1034 (2020).
10. Gao, A. et al. Quantum metric nonlinear Hall effect in a topological antiferromagnetic heterostructure. *Science* **381**, 181–186 (2023).
11. Wang, N. et al. Quantum-metric-induced nonlinear transport in a topological antiferromagnet. *Nature* **621**, 487–492 (2023).
12. Xi, T. et al. Terahertz sensing based on the nonlinear electrodynamics of the two-dimensional correlated topological semimetal $TaIrTe_4$. *Nat. Electron.* **8**, 578–586 (2025).
13. Jiang, H. et al. Probing interplay of topological properties and electron correlation in $TaIrTe_4$ via nonlinear Hall effect. *Nat. Commun.* **16**, 6351 (2025).
14. Cao, Y. et al. Unconventional superconductivity in magic-angle graphene superlattices. *Nature* **556**, 43–50 (2018).
15. Lu, X. et al. Superconductors, orbital magnets and correlated states in magic-angle bilayer graphene. *Nature* **574**, 653–657 (2019).
16. Sharpe, A. L. et al. Emergent ferromagnetism near three-quarters filling in twisted bilayer graphene. *Science* **365**, 605–608 (2019).
17. Serlin, M. et al. Intrinsic quantized anomalous Hall effect in a moiré heterostructure. *Science* **367**, 900–903 (2020).
18. Chen, G. et al. Tunable correlated Chern insulator and ferromagnetism in a moiré superlattice. *Nature* **579**, 56–61 (2020).
19. Regan, E. C. et al. Mott and generalized Wigner crystal states in WSe_2/WS_2 moiré superlattices. *Nature* **579**, 359–363 (2020).
20. Andrei, E. Y. et al. The marvels of moiré materials. *Nat. Rev. Mater.* **6**, 201–206 (2021).
21. Mak, K. F. & Shan, J. Semiconductor moiré materials. *Nat. Nanotechnol.* **17**, 686–695 (2022).
22. Wang, P. et al. One-dimensional Luttinger liquids in a two-dimensional moiré lattice. *Nature* **605**, 57–62 (2022).
23. Kang, K. et al. Switchable moiré potentials in ferroelectric WTe_2/WSe_2 superlattices. *Nat. Nanotechnol.* **18**, 861–866 (2023).
24. Cai, J. et al. Signatures of fractional quantum anomalous Hall states in twisted $MoTe_2$. *Nature* **622**, 63–68 (2023).
25. Zeng, Y. et al. Thermodynamic evidence of fractional Chern insulator in moiré $MoTe_2$. *Nature* **622**, 69–73 (2023).
26. Park, H. et al. Observation of fractionally quantized anomalous Hall effect. *Nature* **622**, 74–79 (2023).
27. Xu, F. et al. Observation of integer and fractional quantum anomalous Hall effects in twisted bilayer $MoTe_2$. *Phys. Rev. X* **13**, 031037 (2023).
28. Lu, Z. et al. Fractional quantum anomalous Hall effect in multilayer graphene. *Nature* **626**, 759–764 (2024).
29. Kang, K. et al. Evidence of the fractional quantum spin Hall effect in moiré $MoTe_2$. *Nature* **628**, 522–526 (2024).
30. Chen, M. et al. Selective and quasi-continuous switching of ferroelectric Chern insulator devices for neuromorphic computing. *Nat. Nanotechnol.* **19**, 962–969 (2024).
31. Wang, Y. et al. Structural phase transition in monolayer $MoTe_2$ driven by electrostatic doping. *Nature* **550**, 487–491 (2017).
32. Forsythe, C. et al. Band structure engineering of 2D materials using patterned dielectric superlattices. *Nat. Nanotechnol.* **13**, 566–571 (2018).
33. Ribeiro-Palau, R. et al. Twistable electronics with dynamically rotatable heterostructures. *Science* **361**, 690–693 (2018).
34. Inbar, A. et al. The quantum twisting microscope. *Nature* **614**, 682–687 (2023).
35. Devarakonda, A. et al. Evidence of striped electronic phases in a structurally modulated superlattice. *Nature* **631**, 526–530 (2024).
36. Tang, H. et al. On-chip multi-degree-of-freedom control of two-dimensional materials. *Nature* **632**, 1038–1044 (2024).
37. Kim, D. S. et al. Electrostatic moiré potential from twisted hexagonal boron nitride layers. *Nat. Mater.* **23**, 65–70 (2024).
38. Porer, M. et al. Non-thermal separation of electronic and structural orders in a persisting charge density wave. *Nat. Mater.* **13**, 857–861 (2014).
39. Comin, R. & Damascelli, A. Resonant X-ray scattering studies of charge order in cuprates. *Annu. Rev. Condens. Matter Phys.* **7**, 369–405 (2016).
40. Vaskivskyi, I. et al. Fast electronic resistance switching involving hidden charge density wave states. *Nat. Commun.* **7**, 11442 (2016).
41. Husremović, S. et al. Encoding multistate charge order and chirality in endotaxial heterostructures. *Nat. Commun.* **14**, 6031 (2023).
42. Kong, L., Shindou, R. & Sun, Z. Fate of transient order parameter domain walls in ultrafast experiments. *npj Quantum Mater.* **10**, 25 (2025).
43. Dzsaber, S. et al. Giant spontaneous Hall effect in a nonmagnetic Weyl–Kondo semimetal. *Proc. Natl Acad. Sci. USA* **118**, e2013386118 (2021).
44. Sinha, S. et al. Berry curvature dipole senses topological transition in a moiré superlattice. *Nat. Phys.* **18**, 765–770 (2022).

45. Huang, Y.-X., Feng, X., Wang, H., Xiao, C. & Yang, S. A. Intrinsic nonlinear planar Hall effect. *Phys. Rev. Lett.* **130**, 126303 (2023).
46. Levin, M. & Stern, A. Fractional topological insulators. *Phys. Rev. Lett.* **103**, 196803 (2009).
47. Maciejko, J. & Fiete, G. A. Fractionalized topological insulators. *Nat. Phys.* **11**, 385–388 (2015).
48. Stern, A. Fractional topological insulators: a pedagogical review. *Annu. Rev. Condens. Matter Phys.* **7**, 349–368 (2016).
49. Neupert, T., Denner, M. M., Yin, J.-X., Thomale, R. & Hasan, M. Z. Charge order and superconductivity in kagome materials. *Nat. Phys.* **18**, 137–143 (2022).
50. Chen, C. et al. Strong electron–phonon coupling in magic-angle twisted bilayer graphene. *Nature* **636**, 342–347 (2024).

Methods

$TaIrTe_4$ crystal growth

High-quality $TaIrTe_4$ crystals were synthesized by a Te flux growth method with a molar ratio of Ta, Ir and Te elements (purity over 99.99%) of 3:3:94 in an alumina crucible and sealed in a vacuum quartz tube. The tube was slowly heated and maintained at 1,373 K for 10 h and then gradually cooled to 873 K at a rate of 1.5 K h^{-1}. The $TaIrTe_4$ single crystals were separated from the Te flux by centrifuging.

$TaIrTe_4$ monolayer fabrication

Monolayer $TaIrTe_4$ was prepared by mechanical exfoliation onto 285-nm-thick SiO_2/Si substrates using the Scotch tape method. Owing to the air sensitivity of thin $TaIrTe_4$ flakes, exfoliation was conducted entirely inside an argon glovebox. Before exfoliation, the SiO_2 substrates were treated with mild oxygen plasma to enhance flake adhesion. The tape carrying exfoliated $TaIrTe_4$ was brought into contact with the substrate and gently pressed to eliminate trapped air bubbles. The stack was then heated at 80 °C for 15 min. After cooling, the tape was carefully peeled off, and monolayer flakes were identified under an optical microscope.

We employed a bottom-contact device architecture with full boron nitride (BN) encapsulation. The fabrication began with the assembly of a bottom-gate stack (few-layer graphene/BN) using a dry-transfer method facilitated by a polycarbonate/polydimethylsiloxane stamp. Residual polymer was removed by thermal annealing at 350 °C for 3 h in a forming gas atmosphere (Ar/H_2) using a tube furnace. Subsequently, metal contacts were patterned using electron-beam lithography (Elionix HS50), followed by deposition of 2 nm of Ti/10 nm of Pt by electron-beam evaporation (Angstrom Engineering). These contacts were then cleaned using both post-annealing and contact-mode tip-cleaning with an atomic force microscope. The prepared contact stack was transferred into an argon glovebox for the remainder of the fabrication. Inside the glovebox, we assembled the top-gate stack (BN/few-layer graphene/BN) using a polycarbonate/polydimethylsiloxane stamp. Monolayer $TaIrTe_4$ flakes were exfoliated, identified, picked up by the top stack and transferred onto the bottom stack—all within a single day—within the glovebox. Finally, to protect the completed device, a poly(methyl methacrylate) capping layer was applied through spin-coating inside the glovebox. See Supplementary Information section 1 for more fabrication details.

Linear and nonlinear Hall transport measurements

The linear (ω) and nonlinear Hall (2ω) transport measurements[51–54] were conducted simultaneously by standard lock-in techniques at a frequency of $\omega = 17.777$ Hz. Gate voltages were applied using Keithley source meters. In dual-gated devices, the carrier densities n and external electric field E can be independently adjusted through the combination of the top-gate voltage (V_{tg}) and bottom-gate voltage (V_{bg}):

$$n = \frac{\epsilon_0 \epsilon_{\mathrm{BN}} V_{\mathrm{bg}}}{e d_{\mathrm{b}}} + \frac{\epsilon_0 \epsilon_{\mathrm{BN}} V_{\mathrm{tg}}}{e d_{\mathrm{t}}}, \tag{2}$$

$$E = \frac{1}{2}\left(\frac{V_{\mathrm{bg}}}{d_{\mathrm{b}}} - \frac{V_{\mathrm{tg}}}{d_{\mathrm{t}}}\right), \tag{3}$$

where ϵ_0 is the vacuum permittivity, ϵ_{BN} is the BN dielectric constant ($\epsilon_{\mathrm{BN}} \approx 3$) and d_{b} (d_{t}) is the thickness of the bottom (top) BN dielectric layer.

Characteristics of the nonlinear Hall response

The nonlinear Hall current $\mathbf{J}^{\mathrm{NLHE}}$ arising from the Berry curvature dipole can be expressed as:

$$\mathbf{J}^{\mathrm{NLHE}} = \frac{e^3 \tau}{2(1 + \mathrm{i}\omega\tau)} \hat{c} \times \mathbf{E}(\mathbf{\Lambda} \cdot \mathbf{E}), \tag{4}$$

where e is the electron charge, τ is the relaxation time, ω is the frequency, $\mathbf{E}$ is the applied electric field and $\mathbf{\Lambda}$ denotes the Berry curvature dipole. Based on equation (4), the following key features are expected: (1) Hall effect: The term $\hat{c} \times \mathbf{E}$ indicates that $\mathbf{J}^{\mathrm{NLHE}}$ is transverse to the applied electric field $\mathbf{E}$, characteristic of a Hall response. (2) Angle dependence: The term ($\mathbf{\Lambda} \cdot \mathbf{E}$) introduces a dependence on the angle between $\mathbf{\Lambda}$ and $\mathbf{E}$. The response is maximized when $\mathbf{\Lambda} \parallel \mathbf{E}$ and vanishes when $\mathbf{\Lambda} \perp \mathbf{E}$. (3) Quadratic I–V: The nonlinear Hall voltage (current) scales quadratically with the applied current $\mathbf{I}$ (electric field $\mathbf{E}$), regardless of signal polarity. (4) Linear scaling between $\sigma_{baa}^{2\omega}$ and σ_{aa}: In our case, the second-order nonlinear Hall conductivity $\sigma_{baa}^{2\omega}$ is given by:

$$\sigma_{baa}^{2\omega} = \frac{j_{baa}^{2\omega}}{(E_{\mathrm{a}})^2} = \frac{e^3 \tau}{2\hbar^2 (1 + \mathrm{i}\omega\tau)} \Lambda, \tag{5}$$

where $j_{baa}^{2\omega}$ is the nonlinear Hall current, E_{a} is the applied electrical field and $\hbar$ is the Planck constant. With $\omega\tau \ll 1$, this simplifies to $\sigma_{baa}^{2\omega} \approx \frac{e^3 \tau}{2\hbar^2} \Lambda$, indicating a linear dependence on the relaxation time τ. From the Drude model, the linear conductivity is given by $\sigma_{aa} = ne^2\tau/m$, which is also proportional to τ, indicating that $\sigma_{baa}^{2\omega} \propto \sigma_{aa}$. Here, m is the electron mass. These criteria have been systematically examined in our measurements, as shown in Extended Data Fig. 1, and we confirmed the Berry curvature origin of the observed responses.

Raman measurements

Raman spectra were taken in a backscattering geometry using a home-built set-up integrated with an Attodry 2100 cryostat, which provided a temperature range from approximately 1.7 K to 300 K. A dual-gated monolayer $TaIrTe_4$ device was loaded into the cryostat, which enabled doping control during the Raman measurements. A 532-nm diode laser (cobalt) or 633-nm He–Ne laser served as the excitation source, with a fixed laser power of 1 mW and an integration time of 200 s per spectrum. Elastic scattering signals were suppressed using a series of notch filters. The Raman set-up enabled us to detect low-energy signals above 20 cm^{-1} with an energy resolution of approximately 0.5 cm^{-1} using an Andor spectrometer equipped with a 1,800 lines per millimetre grating. The polarization was controlled by adjusting the combination of the incident polarizer, quarter-wave plate or half-wave plate angles, and detection analyser. The data shown in the main text were measured in a circular cross-polarized configuration controlled by the quarter-wave plate.

First-principles calculations

The Vienna ab initio simulation package (VASP)[55] was used for the density functional theory (DFT)[56] calculations. The valence electron configurations of Ta, Ir and Te were described with projector augmented-wave pseudopotentials[57], and the electronic interactions were addressed by the Perdew–Burke–Ernzerhof functional[58]. The cutoff of the plane wave was 500 eV, and the width of the Gaussian smearing was 0.05 eV. The k-grid of the Monkhorst–Pack scheme was set to 16 × 6 × 1 for the integrations of the Brillouin zone. For the structural relaxation, the convergence criteria for lattice optimizations were set at 10^{-6} eV and 0.1 meV Å^{-1} for total energy and ionic forces, respectively.

We modelled the superlattice-modulated band structure using a Fröhlich–Peierls Hamiltonian[59] and computed the Berry curvature dipole, finding qualitative agreement with the experimental second-order nonlinear Hall response (Supplementary Information section 3).

Free-energy model

We developed a phenomenological free-energy model with two order parameters (low-energy electronic order and superlattice order) and two external control parameters (doping and temperature). A detailed description of this model and its correspondence with the experiment is provided in Supplementary Information sections 6 and 7. Here we outline the key points. The free energy $F(\varphi, X; T, n)$ takes the following form:

$$F(\varphi, X; T, n) = \frac{1}{2!}a(T, n)\varphi^2 + \frac{1}{4!}\varphi^4 + \frac{1}{2!}\alpha(T)X^2 + \frac{1}{4!}\beta(T)X^4 + \frac{1}{6!}X^6 + \lambda\varphi X. \quad (6)$$

Here φ is the low-energy electronic order, X is the superlattice order, n is the carrier density, T is the temperature and λ is the electron–lattice coupling coefficient. Near the phase transition, the coefficients in equation (6) take the lowest order temperature (T) and carrier density (n) dependence as

$$\alpha(T) = (-c_1T + c_2)^2 + c_3, \quad (7)$$

$$\beta(T) = c_4T - c_5, \quad (8)$$

$$a(T, n) = c_6T - c_7n + c_8. \quad (9)$$

Where the coefficients c_1 to c_8 are constants. We first examine the behaviour of individual order parameters without the coupling. The dependence of the free energy F on the low-energy electronic order φ follows the standard Ginzburg–Landau mean-field theory[60], in which a negative quadratic coefficient $a(T, n) < 0$ leads to spontaneous symmetry breaking of the electronic order (Extended Data Fig. 7a). The anharmonicity of the superlattice distortion X is a central feature of our model. Unlike a simple harmonic lattice, in which distortions are governed by quadratic terms, the potential landscape of a superlattice distortion requires higher order anharmonic terms, such as X^4 and X^6 (Extended Data Fig. 7b). Anharmonicity generally exists in all crystals and molecules, but it is usually neglected, as lattice vibrations are usually confined to the harmonic regime by the steep potential barrier. The anharmonic effects become stronger for superlattices with a long wavelength, which reduces the symmetry, folds the phonon spectrum and leads to a shallower potential surface accessible by electron–phonon coupling.

After analysing the free energy F as a function of individual order parameters, we now examine its behaviour in a two-dimensional order-parameter space. In this extended space, $F(\varphi, X)$ develops several local minima. To illustrate, we start with the decoupled system, that is, $\lambda = 0$ in equation (6). In this limit (Extended Data Fig. 7c), the local minima of the free energy correspond to the Cartesian product of the one-dimensional minima. At a low carrier density far from the VHSs ($n \ll n_e$; Extended Data Fig. 7c, left), the electronic order φ vanishes ($\varphi = 0$) for all local minima and $F(\varphi, X)$ has three local minima, which can be classified based on the superlattice order. We denote the local minima without a superlattice order ($X = 0$) as the type I phase, whereas the minima with a finite superlattice order ($X \neq 0$) are the type II phase.

At a carrier density close to the VHSs ($n \geq n_e$; Extended Data Fig. 7c right), the charge susceptibility is amplified and spontaneous symmetry breaking occurs in the φ part of the free energy. The consequence of this ordering in the context of the free energy $F(\varphi, X)$ is the splitting of these potential wells along the φ (low-energy electronic order) axis. In this case, with the finite electronic order parameter ($\varphi \neq 0$), we denote the minima without and with the superlattice order as type III ($X = 0$) and type IV ($X \neq 0$) phases, respectively.

If the coupling coefficient λ is adiabatically increased from zero to its physical value, the local minima of free energy corresponding to phases I, II, III and IV will be modified accordingly. However, they can still be categorized based on whether they maintain the low-energy electronic order and superlattice order. Note that the electronic order of phase II and the superlattice order of phase III are small but do not exactly vanish due to the finite coupling λ (Extended Data Fig. 7d). The order parameters for the different phases are summarized in Extended Data Fig. 7e.

Extended Data Fig. 7f shows a phase diagram featuring four distinct phases. In phase I, neither the electronic order nor the superlattice is present. This phase resides on the left-hand side of the phase diagram. In phase II, the electronic order is weak, and the superlattice is on (denoted as 1). This phase occupies the left-hand bottom corner of the diagram. Notably, the left-hand bottom corner can host either phase I or phase II, depending on whether the system undergoes φ-field cooling. Both phase III and phase IV correspond to a strong electronic order induced by VHSs and are located on the right-hand half of the diagram. The distinction lies in the superlattice state: phase III corresponds to superlattice off (denoted as 0), whereas phase IV corresponds to superlattice on (1). The upper part of phase III occurs because φ is not large enough to induce the superlattice. The lower part of phase III, which overlaps with phase IV, arises when the cooling path corresponds to no φ cooling.

In this model, the writing force that drives the transition from $X = 0$ to $X \neq 0$ is clearly the coupling term $\lambda\varphi X$, consistent with experimental observations that the $X \neq 0$ phase is triggered by the electronic order at n_e. The reverse transition—from $X \neq 0$ back to $X = 0$—can occur when φ vanishes, provided the barrier between the two states is negligible. There is also the possibility of explicit erasing forces arising from coupling between the superlattice and holes. For instance, DFT calculations indicate the presence of VHSs in the valence band below n_h (refs. 5,61,62), which could stabilize an alternative electronic order with a distinct wavevector Q that competes with the order at n_e. Such competition may generate another erasing force capable of overcoming the barrier and restoring the $X = 0$ state. It would be interesting to explore deeper hole doping towards the valence VHSs, where competing electronic instabilities may stabilize a second superlattice with a distinct periodicity. Observing reversible transitions between the two superlattices would provide strong support for this scenario. We leave this as an open question for future investigation.

Data availability

All data that support the findings of this study are available at https://doi.org/10.7910/DVN/ULKFAE (ref. 63), and from the corresponding author on request. Source data are provided with this paper.

Code availability

All codes that support the findings of this study are available from the corresponding author on request.

51. Du, Z., Lu, H.-Z. & Xie, X. Nonlinear Hall effects. *Nat. Rev. Phys.* **3**, 744–752 (2021).
52. Ortix, C. Nonlinear Hall effect with time-reversal symmetry: theory and material realizations. *Adv. Quantum Technol.* **4**, 2100056 (2021).
53. Adak, P. C., Sinha, S., Agarwal, A. & Deshmukh, M. M. Tunable moiré materials for probing Berry physics and topology. *Nat. Rev. Mater.* **9**, 481–498 (2024).
54. Tang, J. et al. Quantum spin Hall effects in van der Waals materials. *Adv. Quantum Technol.* **8**, e00327 (2025).
55. Kresse, G. & Hafner, J. Ab initio molecular dynamics for liquid metals. *Phys. Rev. B* **47**, 558 (1993).
56. Hohenberg, P. & Kohn, W. Inhomogeneous electron gas. *Phys. Rev.* **136**, B864 (1964).
57. Blöchl, P. E. Projector augmented-wave method. *Phys. Rev. B* **50**, 17953 (1994).
58. Perdew, J. P., Burke, K. & Ernzerhof, M. Generalized gradient approximation made simple. *Phys. Rev. Lett.* **77**, 3865 (1996).
59. Fröhlich, H. On the theory of superconductivity: the one-dimensional case. *Proc. R. Soc. Lond. Ser. A* **223**, 296–305 (1954).
60. McMillan, W. Landau theory of charge-density waves in transition-metal dichalcogenides. *Phys. Rev. B* **12**, 1187 (1975).
61. Lai, J., Zhan, J., Liu, P., Chen, X.-Q. & Sun, Y. Electric field tunable nonlinear Hall terahertz detector in the dual quantum spin Hall insulator TaIrTe$_4$. *Phys. Rev. B* **110**, 155122 (2024).
62. Li, J. et al. Interaction-driven topological transitions in monolayer TaIrTe$_4$. Preprint at http://arxiv.org/abs/2506.18412 (2025).
63. Tang, J. Replication data for: Bistable superlattice switching in a quantum spin Hall insulator. *Harvard Dataverse* https://doi.org/10.7910/DVN/ULKFAE (2026).

Acknowledgements We thank M. Shankar, R. Comin and K.-M. Kim for valuable discussions during the initial Raman measurements. We also thank J. Song, L. Fu, X. Qian, Y. He and Z. Wang for insightful discussions. Q.M. and S.-Y.X. acknowledge support from the Center for the Advancement of Topological Semimetals, an Energy Frontier Research Center funded by the US Department of Energy, Office of Science, through the Ames Laboratory (Contract No. DE-AC02-07CH11358, transport measurements). Q.M. acknowledges support from the AFOSR (Grant Nos. FA9550-22-1-0270 and FA9550-24-1-0117, sample fabrication and data analysis). Q.M. also acknowledges support from the ONR (Grant No. N00014-24-1-2102, optical measurements and manuscript preparation) and from the NSF (CAREER Award No. DMR-2143426, equipment upgrades and maintenance). In addition, Q.M. acknowledges support from the AFOSR DURIP (Award No. FA9550-24-1-0077 for the acquisition of equipment used for Raman measurements). Y.Z. acknowledges support from the Max-Planck partner laboratory grant for quantum materials. The research by J.L. was primarily supported by the NSF Materials Research Science and Engineering Center programme through the UT Knoxville Center for Advanced Materials and Manufacturing (Grant No. DMR-2309083). S.D. and Y.W. acknowledge support from the AFOSR Young Investigator Program (Grant No. FA9550-23-1-0153). Simulation results were obtained using the Frontera computing system at the Texas Advanced Computing Center. Frontera is made possible by NSF Award No. OAC-1818253. Bulk single crystals were grown and $\mathrm{TaIrTe_4}$ was characterized at UCLA, which was supported by the US Department of Energy, Office of Science (Award No. DE-SC0021117). K.S.B. acknowledges support from the AFOSR (Award No. FA9550-24-1-0110). The work of B.S. was supported by the grant DE-SC0018675 funded by the US Department of Energy, Office of Science. STM work is supported by the Office of Basic Energy Science, Materials Science and Engineering Division, US Department of Energy (DOE) under Contract No. DE-SC0012704. K.W. and T. Taniguchi acknowledge support from the JSPS (KAKENHI Grant Nos. 21H05233 and 23H02052), the CREST (Grant No. JPMJCR24A5), JST and the World Premier International Research Center Initiative, MEXT, Japan. We also acknowledge that some of the work was carried out in the Boston College cleanroom and nanotechnology facilities. Work by Z.S. was fully completed during his appointment at Boston College, with support from the Swiss National Science Foundation (Grant No. P500PT-206914).

Author contributions J.T. conducted the experiments under the supervision of Q.M. J.T. fabricated the devices with support from T.S.D., T. Tang, C.Y., M.G., A.G., K.S.B. and S.-Y.X. J.T. performed the transport measurements and analysed the data with contributions from T.S.D., T. Tang, V.B., Zhiheng Huang, Zumeng Huang, Z.S. and M.S. Zumeng Huang built the Raman set-up. J.T. performed the Raman measurements and analysed the data with assistance from T.S.D., B.S., Zhiheng Huang, T. Tang and K.S.B. J.L. and Y.Z. performed the DFT calculations of the band structures and modelled and analysed the superlattice. S.D., N.P., Y.Z. and Y.W. developed the two-order-parameter free-energy model and constructed the phase diagram. X.W. and A.N.P. carried out the scanning tunnelling microscopy characterizations. C.Y., T.Q., C.F. and N.N. grew the bulk $\mathrm{TaIrTe_4}$ crystals. K.W. and T. Taniguchi grew the BN bulk crystals. Q.M., J.T. and S.-Y.X. co-wrote the paper with the input of all authors.

Competing interests The authors declare no competing interests.

Additional information

Supplementary information The online version contains supplementary material available at https://doi.org/10.1038/s41586-026-10309-w.

Correspondence and requests for materials should be addressed to Qiong Ma.

Peer review information *Nature* thanks Cong Xiao and the other, anonymous, reviewer(s) for their contribution to the peer review of this work.

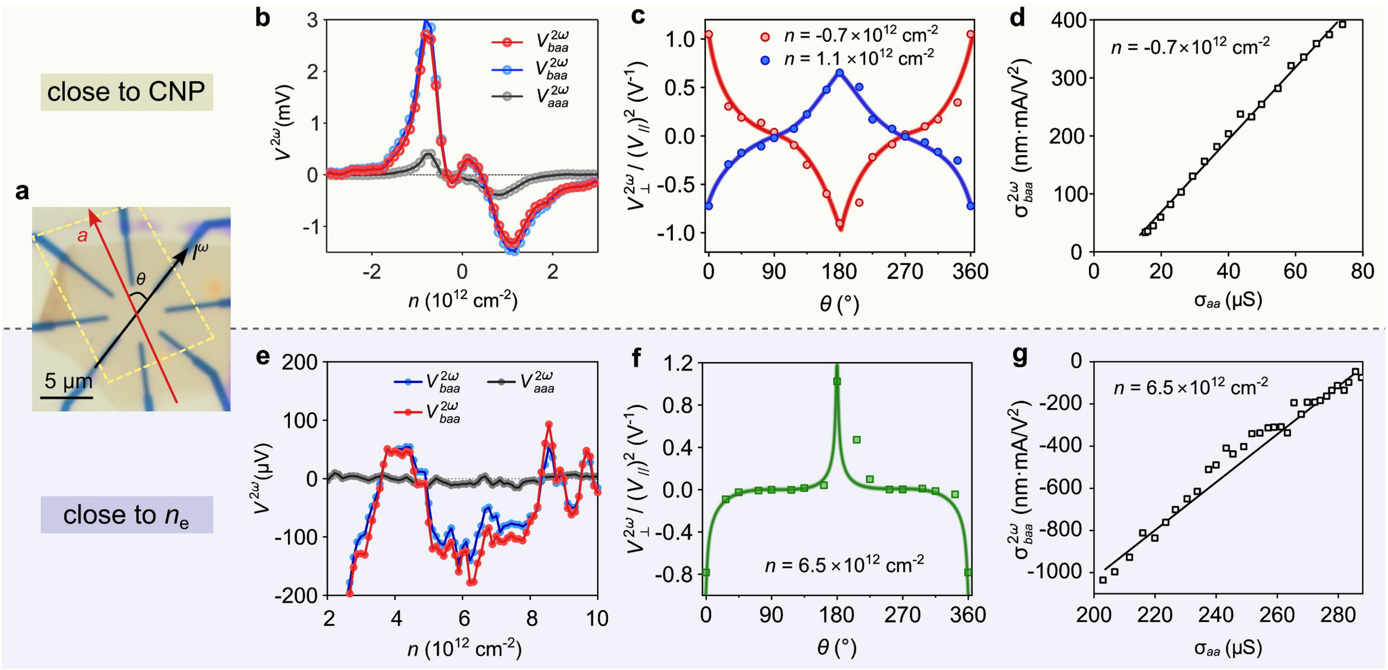

Extended Data Fig. 1 | Key characteristics of Berry curvature nonlinear Hall responses. a, Optical image of Device 1, scale bar, 5 *μ*m. **b**–**d**, Characteristics of the nonlinear Hall response close to the CNP: (1) The longitudinal $V^{2\omega}_{aaa}$ is smaller than $V^{2\omega}_{baa}$. Note that the two $V^{2\omega}_{baa}$ curves are measured from two parallel sets of Hall probes and exhibit highly consistent results. (2) Angular dependence of the nonlinear Hall response $V^{2\omega}$, consistent with the mirror symmetry $\mathcal{M}_a$. Here, θ represents the angle between the crystal axis ($\hat{a}$ direction) and the injection current direction I^{ω}, as illustrated in panel **a**. (3) The scaling relationship between the nonlinear Hall conductivity $\sigma^{2\omega}_{baa}$ and the Drude conductivity σ_{aa} is investigated. $\sigma^{2\omega}_{baa}$ can be obtained from: $\sigma^{2\omega}_{baa} \sim \frac{V^{2\omega}_{baa}\, l}{I_a^2\, R_{aa}^3}$, where I_a is the injected current along $\hat{a}$, R_{aa} is the longitudinal resistance, and l is the sample length, respectively. The observed linear relationship between $\sigma^{2\omega}_{baa}$ and σ_{aa} indicates that $\sigma^{2\omega}_{baa}$ depends linearly on τ, consistent with the Berry curvature-induced nonlinear Hall effect. **e**–**g**, Similar characteristics are observed close to $n = n_{\mathrm{e}}$. Notably, the angular dependence is interestingly sharper.

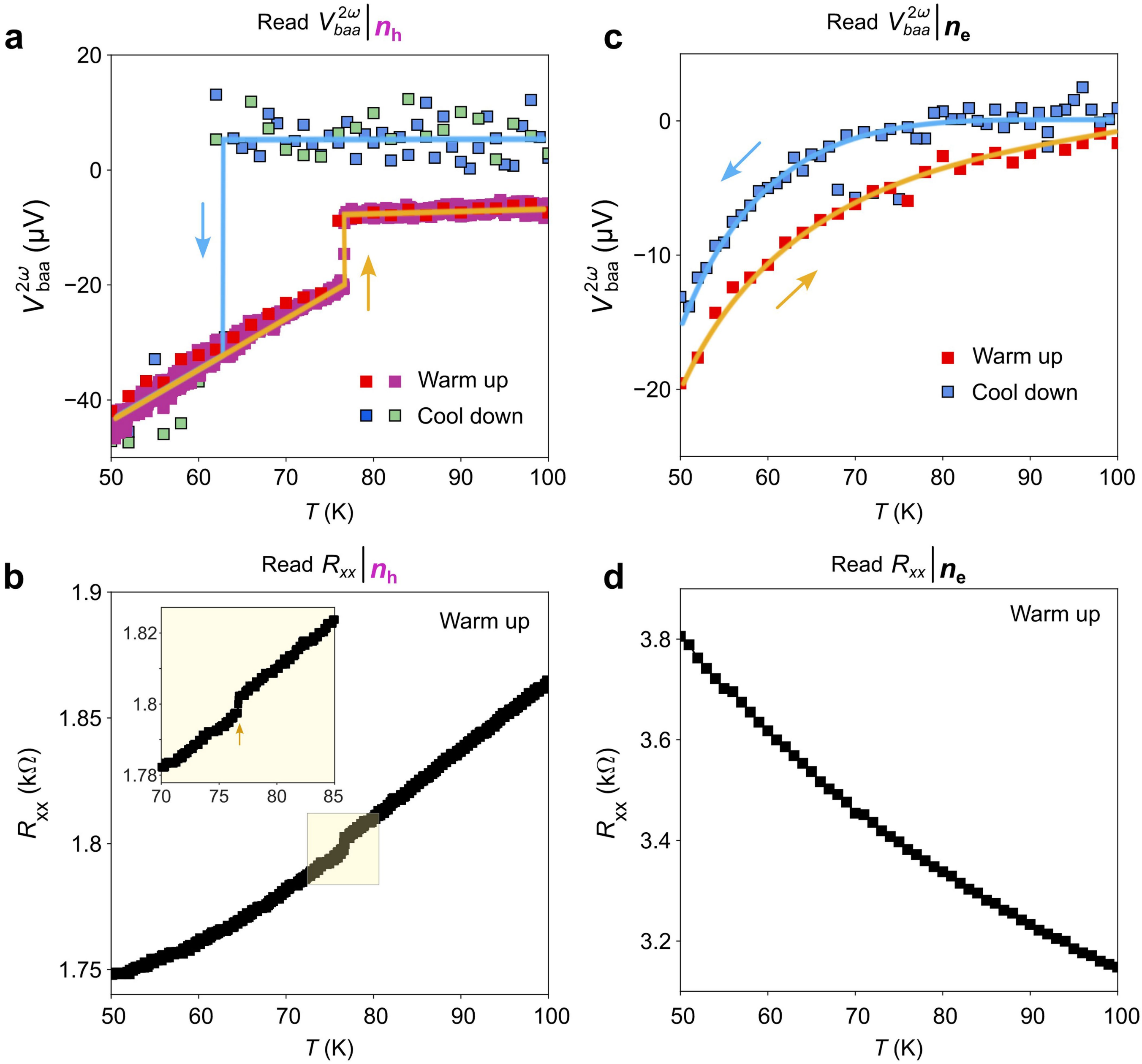

Extended Data Fig. 2 | Temperature dependence of nonlinear Hall and linear resistance responses at n_h and n_e. **a**, Temperature dependence of $V_{baa}^{2\omega}$ at n_h. The cooldown measurement is not straightforward because, to trigger the n_h response during cooling, the carrier density must first be tuned to n_e or above. The corresponding measurement protocol and raw data are shown in Extended Data Fig. 4d (left). The warm-up measurement is more straightforward, as the system is prepared in the ON state and held at fixed n_h. **b**, Temperature dependence of R_{xx}, as the system is prepared in the ON state and held at fixed n_h. Inset shows a zoomed-in view of the resistance jump near T ~ 76 K. **c**,**d**, Temperature dependence of $V_{baa}^{2\omega}$ and R_{xx} at n_e.

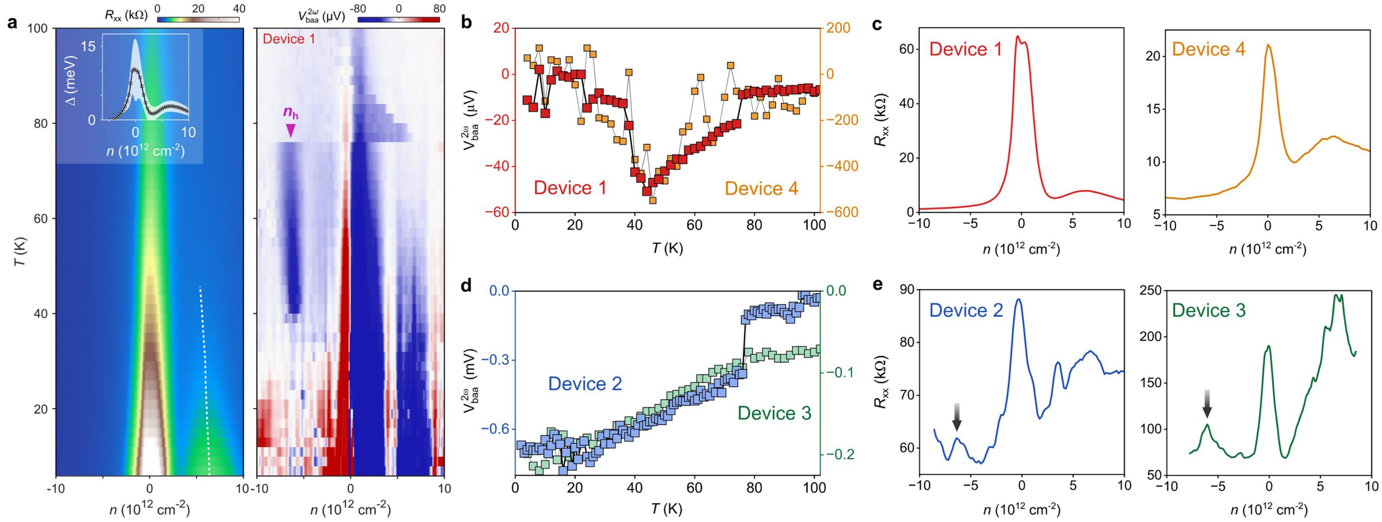

Extended Data Fig. 3 | Observations of R_{xx} and $V_{baa}^{2\omega}$ below 40 K. **a**, Simultaneously measured R_{xx} and $V_{baa}^{2\omega}$ as functions of n and T for Device 1, similar to Fig. 2b,e but extended to 4 K. The white dotted line labels the R_{xx} peak near n_e, which shifts to lower carrier density as the temperature increases from 4 K to 40 K. The extracted gap sizes (inset of the left panel) are smaller than those reported in ref. 5, likely due to enhanced inhomogeneity associated with the larger sample size used here, as well as strain effects[62]. **b**,**c**, In Devices 1 and 4, $V_{baa}^{2\omega}|n_h$ is suppressed below ~40 K, and no R_{xx} peak at n_h (**c**). **d**,**e**, In Devices 2 and 3, $V_{baa}^{2\omega}|n_h$ persists down to 4 K, accompanied by a R_{xx} peak at n_h (**e**, marked by the black arrows). Based on these empirical observations, together with DFT calculations[5,61,62] showing hole-side valence-band VHSs at higher doping, we speculate that the suppression of $V_{baa}^{2\omega}|n_h$ observed below 40 K reflects a redistribution of Berry curvature driven by correlation effects near the hole-side VHSs. In Devices 1 and 4, no sizable gap is present at $n = n_h$, making the system more susceptible to such redistribution, with the suppression of $V_{baa}^{2\omega}|n_h$ as a possible consequence. In contrast, in Devices 2 and 3, the presence of a gap at $n = n_h$ may stabilize the electronic structure and Berry curvature against additional correlation effects arising from the hole-side VHSs. Further investigation is needed to fully understand this interesting observation. Note that the gap observed at n_h in Devices 2 and 3 appears only when the device is cooled from densities near the electron-side VHS, consistent with the superlattice mechanism linked to the electron-side VHS.

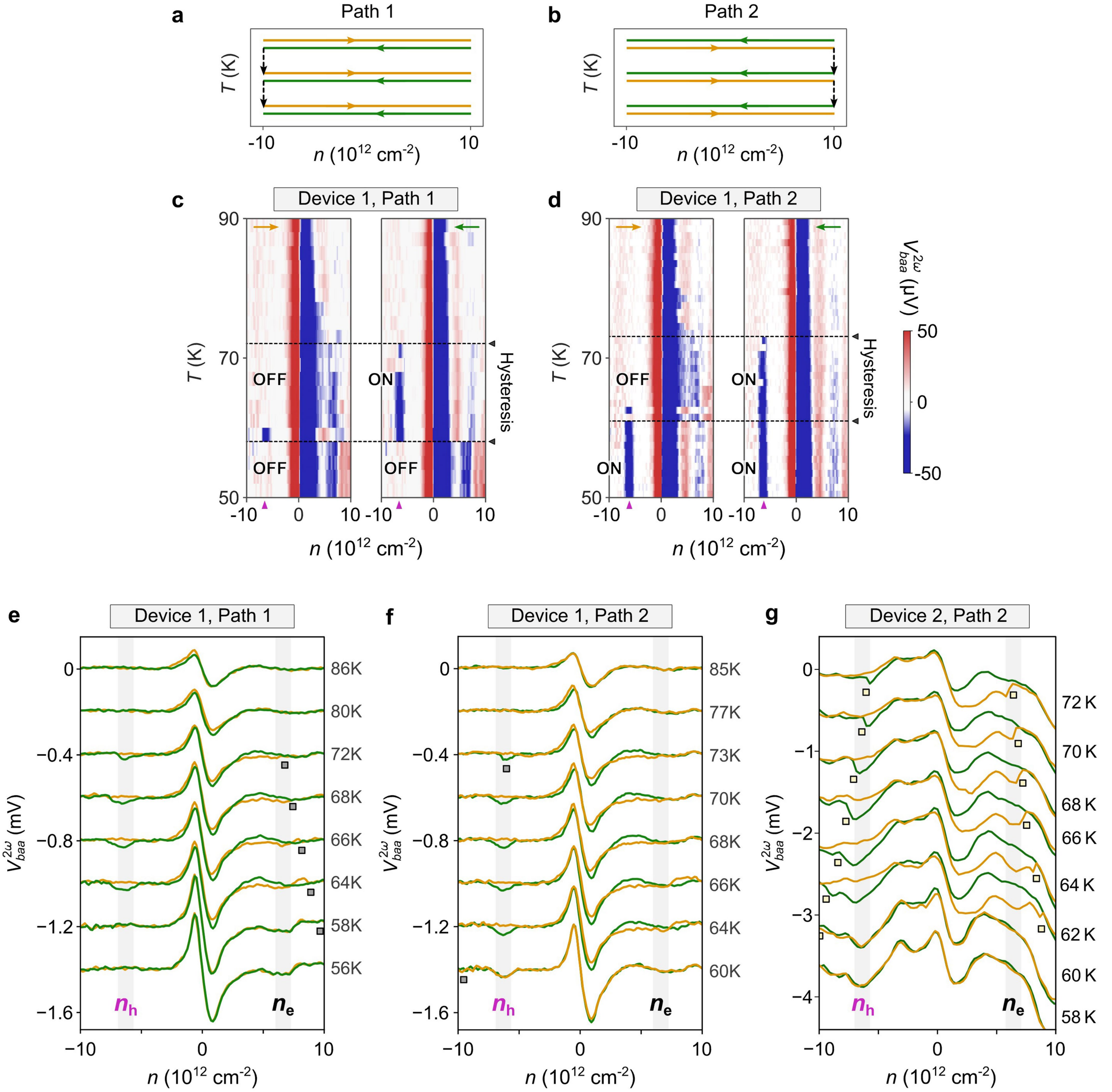

Extended Data Fig. 4 | Systematic hysteretic measurements of the hidden state during cooling. **a**,**b**, The temperature is stepped down at $n = -10 \times 10^{12}$ cm^{-2} (**a**, Path 1) and $n = +10 \times 10^{12}$ cm^{-2} (**b**, Path 2). At each temperature, both forward and backward doping scans are performed to determine the switching points, identified as the densities at which the forward and backward sweeps begin to merge. These points define the critical write boundary for the hidden-state transition from OFF → ON and the erase boundary for the transition from ON → OFF. **c**,**d**, $V_{baa}^{2\omega}$ maps of Device 1 measured following Path 1 and Path 2. A hysteresis window develops upon cooling (72-60 K for Path 1; 73-61 K for Path 2), and the device ultimately stabilizes to distinct final states: $V_{baa}^{2\omega}|n_h$ OFF state (**c**, Path 1); ON state (**d**, Path 2). **e**,**f**, Hysteresis linecuts from panels **c**,**d** for Device 1. The gray square marks the write (OFF → ON) boundary (**e**, Path 1) and the erase (ON → OFF) boundary (**f**, path 2). **g**, Hysteresis measurement of Device 2 following Path 2, with the write (OFF → ON) and erase (ON → OFF) boundaries indicated by light yellow squares.

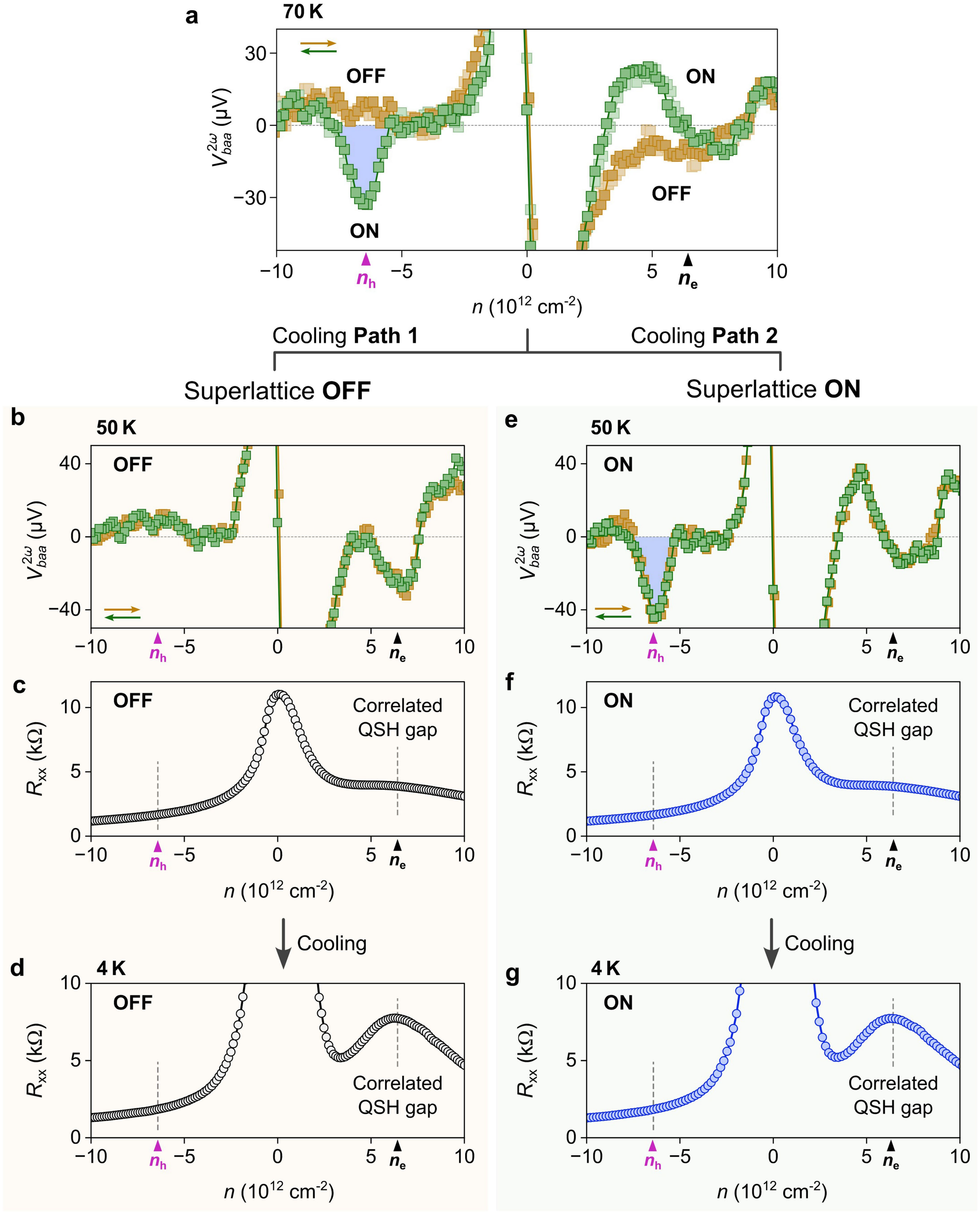

Extended Data Fig. 5 | Demonstration of robust ON state of the correlated insulating phase at n_e. **a**–**d**, Starting from 70 K, the system is cooled along path 1 (cooling with doping away from the VHSs), programming the hidden state to OFF at low temperatures. As shown, $V_{baa}^{2\omega}|n_h$ is nearly zero, while the correlated QSH gap at n_e remains robustly ON, as evidenced by R_{xx}. **e**–**g**, Similar to panels **b**–**d**, but following cooling path 2 (cooling above the VHSs), which programs the hidden state to ON at low temperatures. In this case, $V_{baa}^{2\omega}|n_h$ is large, while the correlated QSH gap at n_e remains ON, as again indicated by R_{xx}.

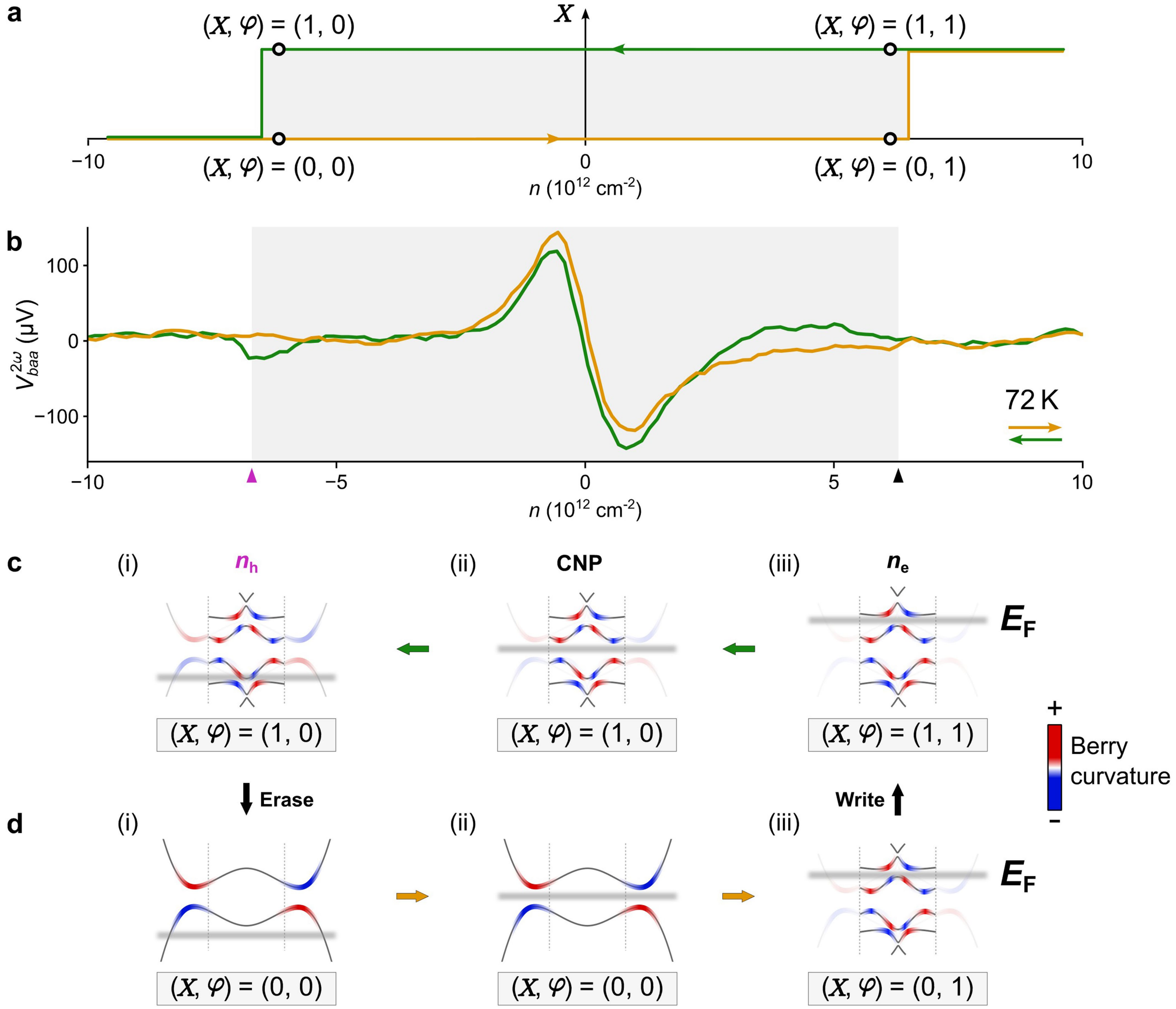

Extended Data Fig. 6 | Superlattice ON-OFF contrast in the nonlinear Hall and linear resistance responses at different carrier densities. **a**,**b**, Schematic illustration of the superlattice memory effect and the associated hysteretic $V_{baa}^{2\omega}$ responses programmed by doping scans. **c**, In the superlattice ON state, band folding induced by the superlattice order persists over a wide density range, encompassing both n_h and n_e. **d**, In the superlattice OFF state, the band structure remains pristine and unfolded at n_h and near the CNP, and becomes folded only when the doping is tuned to n_e due to the electronic order. The two lattice states therefore result in density-dependent ON-OFF contrast. At n_h, the OFF state lacks Berry curvature hot spots, resulting in a nearly zero $V_{baa}^{2\omega}$ response, whereas the ON state exhibits band folding with emergent Berry curvature hot spots, producing a large $V_{baa}^{2\omega}$ response and thus a strong ON-OFF contrast. Near the CNP, Berry curvature hot spots already exist in the OFF state due to the topological gap at the CNP; superlattice formation only weakly modifies the band structure and redistributes the Berry curvature, resulting in a small ON-OFF contrast in $V_{baa}^{2\omega}$. Near n_e, electronic order alone induces band folding and Berry curvature hot spots even in the OFF state, while the lattice order provides an additional modulation, yielding a modest ON-OFF contrast in $V_{baa}^{2\omega}$. Similarly, at other carrier densities, switching between the superlattice ON and OFF states modifies the band structure and redistributes the Berry curvature, thereby producing measurable experimental contrast.

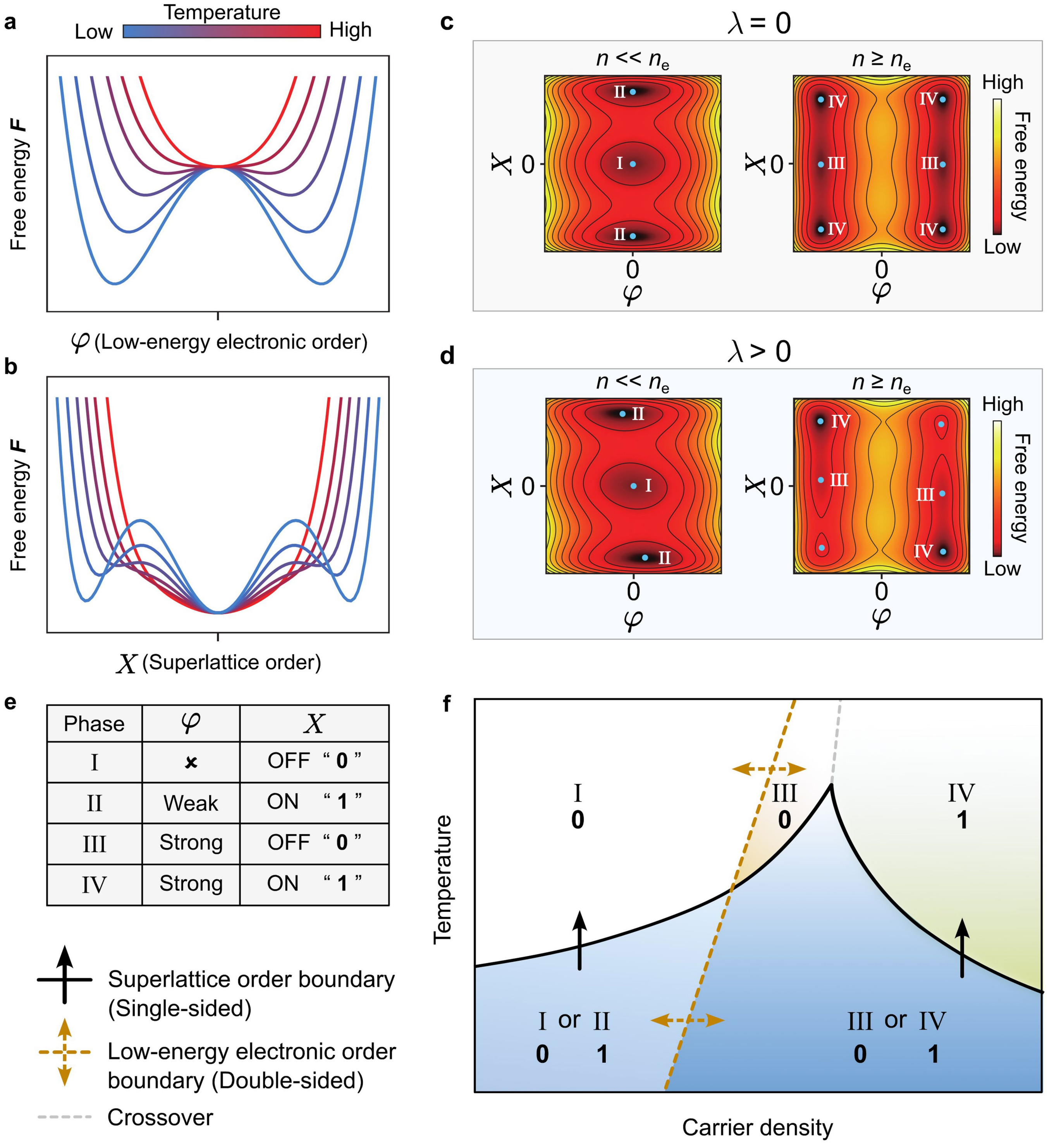

Phase	φ	X
I	×	OFF “ **0** ”
II	Weak	ON “ **1** ”
III	Strong	OFF “ **0** ”
IV	Strong	ON “ **1** ”

Extended Data Fig. 7 | Construction of the phase diagram from the free-energy model. a, Dependence of the free energy F on the low-energy electronic order φ, with the superlattice order fixed at $X = 0$. **b**, Dependence of the free energy F on the superlattice order X, with the low-energy electronic order fixed at $\varphi = 0$. **c**, In the decoupled regime ($\lambda = 0$), the local minima (phases) of the free energy F are classified as Phase I (no electronic order, no superlattice order) and Phase II (no electronic order, with superlattice order) at low carrier density ($n \ll n_e$); and Phase III (with electronic order, no superlattice order) and Phase IV (with electronic order, with superlattice order) at high carrier density ($n \geq n_e$). **d**, Free-energy landscapes at finite coupling $\lambda > 0$. **e**, Summary of the distinct phases determined by the low-energy electronic order φ and superlattice order X. **f**, Phase diagram: the black solid line represents the phase boundary of the superlattice. Above this boundary, the superlattice order has only one phase (‘1’ or ‘0’); below the boundary, it is bistable, depending on the history. When crossing the boundary from above to below, the superlattice order remains unchanged. However, when crossing from below to above, the superlattice order transitions to the phase above. The yellow dashed line marks the phase boundary of the low-energy electronic order, which is second-order and exhibits no hysteresis. On the left side of this boundary, there is no electronic order or only weak electronic order (due to coupling with the lattice); on the right side, the electronic order is present. The grey dashed line represents a crossover in the superlattice order, rather than a true phase transition.

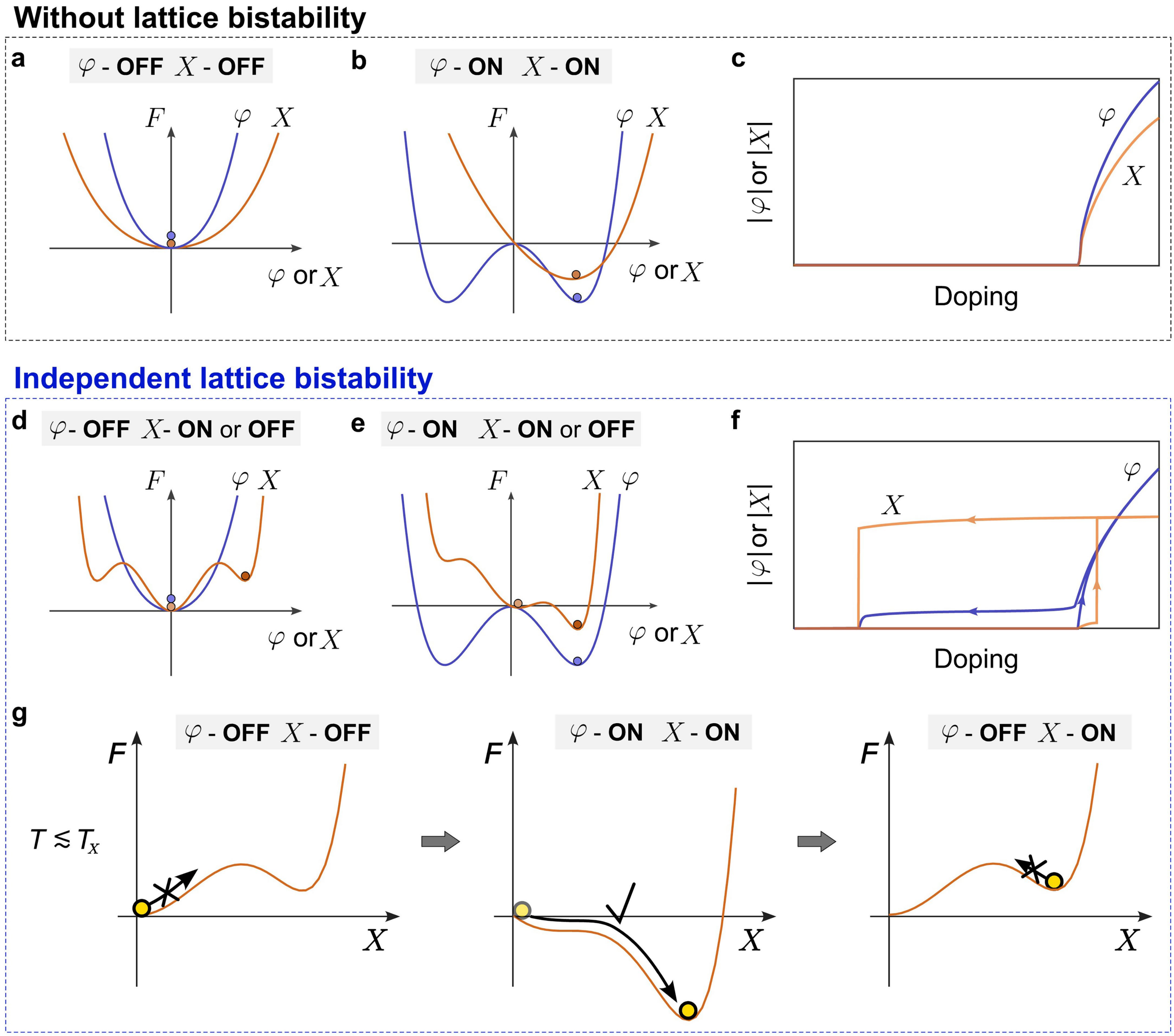

Extended Data Fig. 8 | Comparison of free-energy models without and with independent lattice bistability. a–c, Without lattice bistability: We first consider a lattice free energy F_{Lattice} with a single minimum, modeled as a purely parabolic potential $F_{\mathrm{Lattice}}(X\,;T) = \frac{1}{2}\alpha(T)X^2$, for which the lattice order is strictly slaved to the electronic order: when $\varphi = 0$, $X = 0$, and when $\varphi \neq 0$, coupling to φ shifts the minimum to a finite X. Extending F_{Lattice} to a fourth-order polynomial, $F_{\mathrm{Lattice}}(X\,;T) = \frac{1}{2}\alpha(T)X^2 + \frac{1}{4!}\beta(T)X^4$, yields a unique $X \neq 0$ ground state at low temperature, where coupling to φ only renormalizes the lattice distortion in a reversible manner. In both cases, no intrinsic bistability or hysteresis is supported, inconsistent with the experimentally observed conditional emergence of the $X \neq 0$ state only when φ is activated by doping. **d–f, Independent lattice bistability:** We next consider the model discussed in the main text, where F_{Lattice} is described by a sixth-order polynomial supporting two locally stable minima at $X = 0$ and $X \neq 0$, separated by a finite energy barrier (the sign or phase of X is not distinguished). This intrinsic bistability allows the lattice order to exist in either configuration independently of φ: both $X = 0$ and $X \neq 0$ are locally stable for $\varphi = 0$ and for $\varphi \neq 0$. The coupling term $\lambda\varphi X$ tilts the free-energy landscape, enabling transitions between the two lattice states, while the finite barrier gives rise to pronounced hysteresis. **g**, Schematic evolution of the lattice free-energy landscape versus doping. Electron doping induces a finite electronic order φ, which lowers the $X \neq 0$ minimum via φX coupling and enables barrier crossing from $X = 0$ into $X \neq 0$. Upon removing φ, the barrier persists, trapping the system in the $X \neq 0$ configuration and producing hysteretic, nonvolatile lattice behavior.

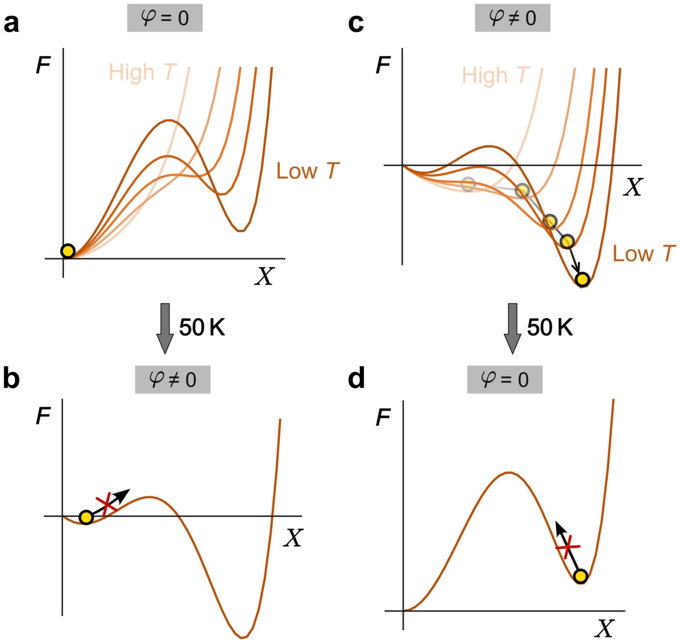

Extended Data Fig. 9 | Free-energy evolution of the lattice order *X* during the 'doping + cooling' process. a,**b**, Cooling at $n < n_e$, i.e., in the absence of φ, the free-energy landscape favors the $X = 0$ minimum, and the system will naturally fall into the superlattice OFF state. **c**,**d**, Cooling at $n \geq n_e$, i.e., in the presence of φ, the coupling term φX tilts the free-energy landscape, making the $X \neq 0$ state the global minimum. As a result, the system settles into the superlattice ON state. At low temperatures, the energy barrier separating the $X = 0$ and $X \neq 0$ minima increases and becomes sufficiently large that the coupling term φX is no longer strong enough to drive transitions between the two states. Consequently, if the system cools into the $X = 0$ state, it remains trapped there even when φ is subsequently applied (**b**); conversely, if the system cools into the $X \neq 0$ state in the presence of φ, removing φ does not restore the $X = 0$ state, again due to the large energy barrier that must be overcome (**d**). In this low-temperature regime, the system is therefore effectively locked into whichever lattice state is selected during cooling.

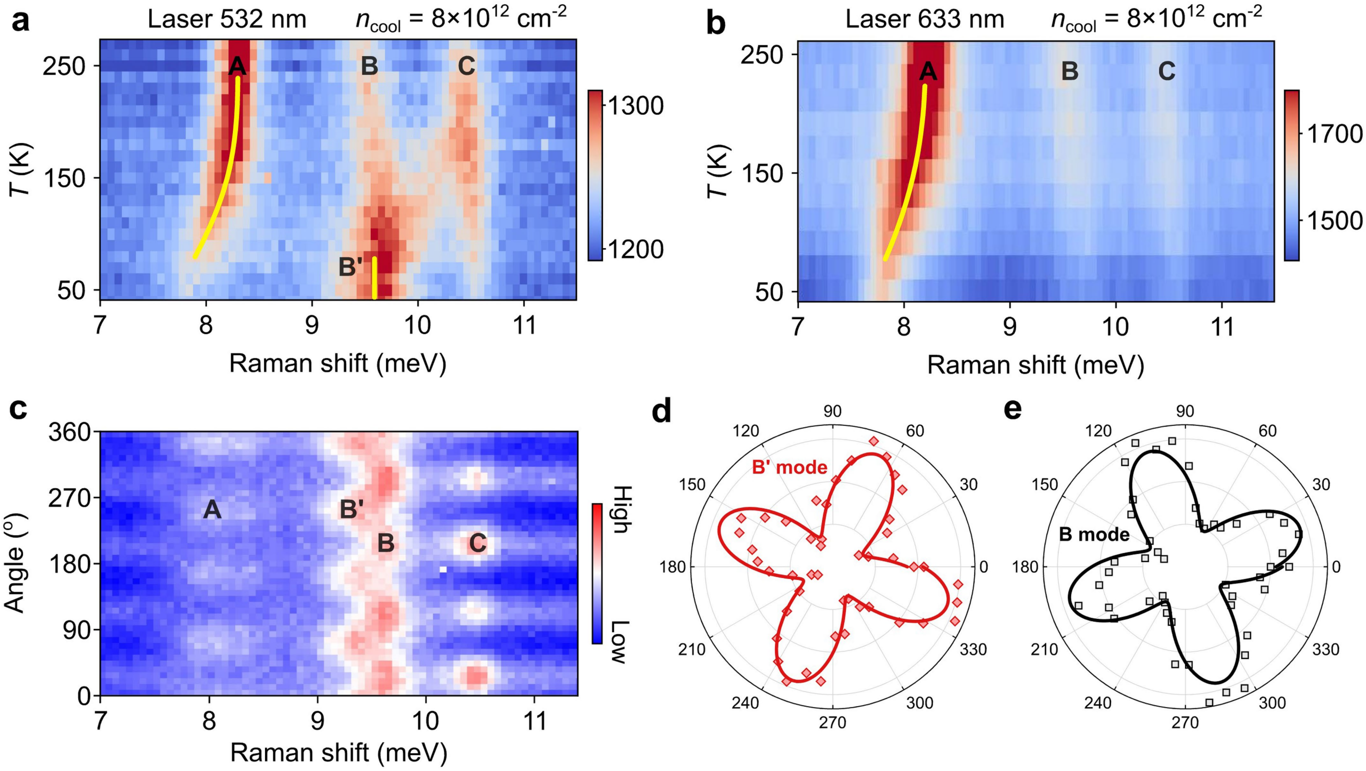

Extended Data Fig. 10 | Additional Raman evidence of B′ mode. a, Raman intensity map measured in the left-right (L-R) circular polarization configuration using a 532 nm excitation laser during cooling from 270 K to 40 K at a fixed carrier density of $n_{\text{cool}} = 8 \times 10^{12}$ cm^{-2}. **b**, Raman intensity map measured under identical cooling and doping conditions using a 633 nm excitation laser. In both cases, three Raman modes (A, B, and C) are observed at high temperature, with mode A softening upon cooling. Notably, mode B′ is selectively enhanced under 532 nm excitation and is absent under 633 nm excitation, indicating a resonant enhancement effect. **c**, Angle-dependent Raman spectra measured in the linear cross-polarization configuration (X-Y), where the angle of incident and scattered light polarization is controlled using half-wave plate, while keeping the polarizer and analyzer fixed in orthogonal position. Four distinct modes (A, B, B′, and C) are clearly resolved. **d**,**e**, Polarization-angle dependence of modes B′ and B, revealing distinct symmetry behaviors and confirming that B and B′ correspond to separate Raman modes. Additional Raman data and discussions are provided in SI Section 8.